Astron. Astrophys. 348, 950–971 (1999)

ASTRONOMY AND ASTROPHYSICS

ORFEUS spectroscopy of the O VI lines in symbiotic stars and the Raman scattering process⋆

H.M. Schmid[1], J. Krautter[1], I. Appenzeller[1], J. Barnstedt[2], T. Dumm[3], A. Fromm[2], M. Gölz[2], M. Grewing[2,4], W. Gringel[2], C. Haas[2], W. Hopfensitz[2], N. Kappelmann[2], G. Krämer[2], A. Lindenberger[2], H. Mandel[1], U. Mürset[3], H. Schild[3], W. Schmutz[3], and H. Widmann[2]

[1] Landessternwarte Heidelberg-Königstuhl, D-69117 Heidelberg, Germany
[2] Institut für Astronomie und Astrophysik der Universität Tübingen, Waldhäuserstrasse 64, D-72076 Tübingen, Germany
[3] Institut für Astronomie, ETH Zentrum, CH-8092 Zürich, Switzerland
[4] Institut de Radio Astronomie Millimétrique (IRAM), 300 Rue de la Piscine, F-38406 Saint Martin d'Hères, France

Received 24 August 1998 / Accepted 16 April 1999

Abstract. We present ORFEUS spectra of the O VI $\lambda\lambda$1032,1038 emission lines in the symbiotic stars AG Dra, V1016 Cyg, RR Tel, CD$-43°14304$, AG Peg and Z And. The O VI emission lines can convert into broad and highly polarized emission lines at λ6825 and λ7082 in a Raman scattering process by neutral hydrogen. From a comparison of direct and Raman scattered radiation we extract new information on the scattering geometry in symbiotic systems.

The nebular O VI emission lines are in all objects redshifted by about $+40$ km s^{-1}. This can be explained as a radiative line transfer effect in a slowly expanding emission region. A comparable redshift is measured in the Raman scattered O VI lines. In AG Peg the O VI emissions show beside a narrow nebular line a broad component from a fast stellar wind outflow.

Many interstellar absorption lines of molecular hydrogen are detected, particularly near the O VI λ1038 component. With model calculations we investigate their impact on the O VI lines.

From the dereddened line fluxes of the direct and Raman scattered O VI lines we derive the scattering efficiency, which is defined as photon flux ratio $N_{\rm Raman}/N_{\rm O\,VI}$. The efficiencies derived for RR Tel, V1016 Cyg and Z And indicate that about 30% of the released O VI λ1032 photons interact with the neutral scattering region. The efficiencies for AG Dra and CD$-43°14304$ are much higher, which may suggest that the O VI nebulosity is embedded in a H^0-region.

The D-type system RR Tel shows strong line profile differences between the direct O VI emission, which is single–peaked, and the Raman scattered emission, which is double–peaked. This indicates that the neutral scattering region in RR Tel "sees" different O VI line profiles, implying that the O VI nebulosity is far from spherically symmetric. In a tentative model we suggest for RR Tel an O VI flow pattern where material streams from the cool giant towards the hot component, which further accelerates the gas radially.

For the S-type systems AG Dra, CD$-43°14304$ and Z And the line profile differences between the direct and the Raman scattered O VI emissions are less pronounced. This may suggest that the O VI profiles depend less on the emission direction than in the D-type system RR Tel.

For AG Peg we detect for the first time the Raman scattered emission at λ6825. The Raman line shows a narrow, nebular component as the O VI line, but no equivalent emission to the broad O VI wind component. The higher conversion efficiency for the narrow component indicates that the nebular O VI emission is significantly closer to the cool giant than the hot, mass losing component, and strongly supports previous colliding wind models for this object.

Key words: stars: binaries: symbiotic – stars: circumstellar matter – stars: mass-loss – polarization – scattering – ultraviolet: stars

1. Introduction

Symbiotic stars are interacting binary systems consisting of a red giant and a hot component, in most cases a hot white dwarf. These binaries show a wide range of interaction processes, such as irradiation and reflection effects, nova-like outbursts, colliding stellar winds and non-spherical mass outflows. These phenomena have been studied observationally and theoretically but many investigations suffer from a severe lack of knowledge on the overall system geometry (see Mikolajewska 1997).

Symbiotic stars often show two strong emission lines at λ6825 and λ7082, which have been identified as Raman scattering of the O VI resonance doublet $\lambda\lambda$1032,1038 by neutral hydrogen (Schmid 1989). These lines provide a new and powerful diagnostic tool for determining the geometric structure of symbiotic systems.

Send offprint requests to: H.M. Schmid, Heidelberg (hschmid@lsw.uni-heidelberg.de)

⋆ Based on observations taken during the ORFEUS-SPAS I and ORFEUS-SPAS II space shuttle missions, and ground based data collected at the ESO 2.2m and 3.6m telescopes at La Silla, Chile, and the 4.2m William Herschel Telescope at La Palma, Canary Islands. ESO observations were granted for the programs 52.7-040 and 58.D-0866.

Spectropolarimetric observations revealed that the Raman lines are strongly polarized (Schmid & Schild 1994; Harries & Howarth 1996b). From the polarization angle we can derive the relative orientation of the light source and the scattering region on the sky. In symbiotic binaries the O VI region is expected to be close to the hot component and plenty of H^0 is found near the cool component. Thus the polarization angle provides the orientation of the binary axis. Observations indeed confirm this picture and show a phase-locked rotation of the polarization which can be used for deriving the orientation and the inclination of the orbital plane (e.g. Harries & Howarth 1996a; Schild & Schmid 1997; Schmid & Schild 1997a,b). This information is particularly interesting for systems with extended nebular structures in order to distinguish between equatorial or polar outflows.

In addition, the Raman lines show often a spectropolarimetric structure through the line profiles, which can be explained by the Doppler shifts introduced by the motion of the scattering H^0-atoms. Thus we can distinguish position angles between scattering regions which move towards the O VI zone and those which move away from it. This provides a unique tool for the investigation of the geometric and dynamic structure of the H^0-scattering region close to the red giant (e.g. Schild & Schmid 1996,1997).

Monte Carlo simulations based on a rotationally symmetric scattering model are able to reproduce the general properties of the Raman line structure (Schmid 1996; Harries & Howarth 1997; Lee & Lee 1997). However, there are discrepancies which indicate that symbiotic systems are not rotationally symmetric. The comparison between observations and model calculations allows first conclusions about the 3-dimensional structure of symbiotic systems (see Schmid 1998).

A problem in previous investigations of the O VI Raman scattering process is the lack or the scarcity of far UV O VI line observations. For symbiotic systems there exist up to now only a few spectra from the ASTRO-II space shuttle mission (Espey et al. 1995; Birriel et al. 1998) and some data from the two VOYAGER spacecrafts (e.g. Li & Leahy 1997).

In this paper we describe spectroscopic observations of symbiotic systems in the far UV taken with ORFEUS. This instrument provides O VI $\lambda\lambda$1032,1038 line observations with an unprecedented spectral resolution and quality. In particular, it is for the first time possible to investigate the O VI line structure. The O VI data are complemented by ground-based observations of the Raman scattered O VI emissions. This allows a detailed comparison of line fluxes and spectral structure between the direct O VI emission and the corresponding Raman scattered emission. Finally we examine the results and discuss conclusions on the geometry of symbiotic systems.

2. Far-ultraviolet observations of the O VI lines

The O VI lines of several symbiotic stars were observed during the ORFEUS-SPAS I and ORFEUS-SPAS-II space shuttle mission STS-51 in September 1993 and STS-80 in November/December 1996 respectively. The ORFEUS telescope (Orbiting Retrievable Far and Extreme Ultraviolet Spectrometer) contains a 1 m normal-incidence primary mirror that feeds two instruments, the Berkeley spectrometer and the Echelle spectrometer (see e.g. Grewing et al. 1998).

2.1. Berkeley spectrograph data

The symbiotic systems AG Dra, AG Peg, RR Tel and Z And were observed during the ORFEUS-I flight and V1016 Cyg and RR Tel during the ORFEUS-II flight with the Berkeley spectrograph (see Table 1). As RR Tel was employed during the second flight for calibration purposes its spectrum has been recorded several times.

Our Berkeley spectra cover the wavelength band from about 900 Å to 1200 Å with a resolution of about $\lambda/\Delta\lambda = 3000$. The wavelength scale carries an uncertainty of about 0.5 Å caused by the unknown location of the target within the 20″ aperture. Relative wavelengths are reliable to about $\pm$ 0.15 Å between 920 Å and 1220 Å. Details on the performance of the Berkeley spectrograph and the standard flux and wavelength calibration of the data can be found in Hurwitz & Bowyer (1995) and Hurwitz et al. (1998).

Spectra of the O VI emission line region of RR Tel, V1016 Cyg, AG Dra, Z And and AG Peg as measured by the Berkeley spectrograph are plotted in Figs. 1 and 3. The spectra have been rebinned to a wavelength step of 0.1 Å, which is about one third of the spectral resolution.

In RR Tel, the O VI emission lines are extremely bright and a spill-over effect had to be corrected additionally in the ORFEUS-II data of the Berkeley spectrograph. Due to the high count rates in the O VI lines the registered photons were smeared perpendicular to the dispersion direction on the 2-dimensional detector map. Thus, O VI counts are registered in the two 3 pixel wide background strips located on both sides of the 7 pixel wide spectral window. To correct for this effect, the line photons in the background strips have been added to the counts in the spectral strip and the mean background counts of adjacent, uncontaminated regions is used for the background correction in the O VI region. Despite this correction, the comparison with the RR Tel spectrum obtained quasi-simultaneously with the Echelle spectrograph suggests that the O VI λ1032 line flux in the Berkeley spectra is still too low by about 20% due to saturation (see Sect. 3.2). The same effect is most likely negligible in the ORFEUS-I data, due to the lower efficiency and the wider extraction window used in the standard reduction procedure (M. Hurwitz, personal communication).

2.2. Echelle spectra

Echelle spectra have been taken for the symbiotic systems RR Tel, AG Dra, AG Peg, Z And and CD$-43^\circ 14304$ during the ORFEUS-II flight. The spectral resolution is better than $\lambda/\Delta\lambda = 10000$ for the covered region $\lambda 900 - \lambda 1400$. Figs. 2 and 3 show the O VI emission line structures of the symbiotic systems RR Tel, AG Dra, Z And, CD$-43^\circ 14304$ and AG Peg taken with the Echelle spectrograph.

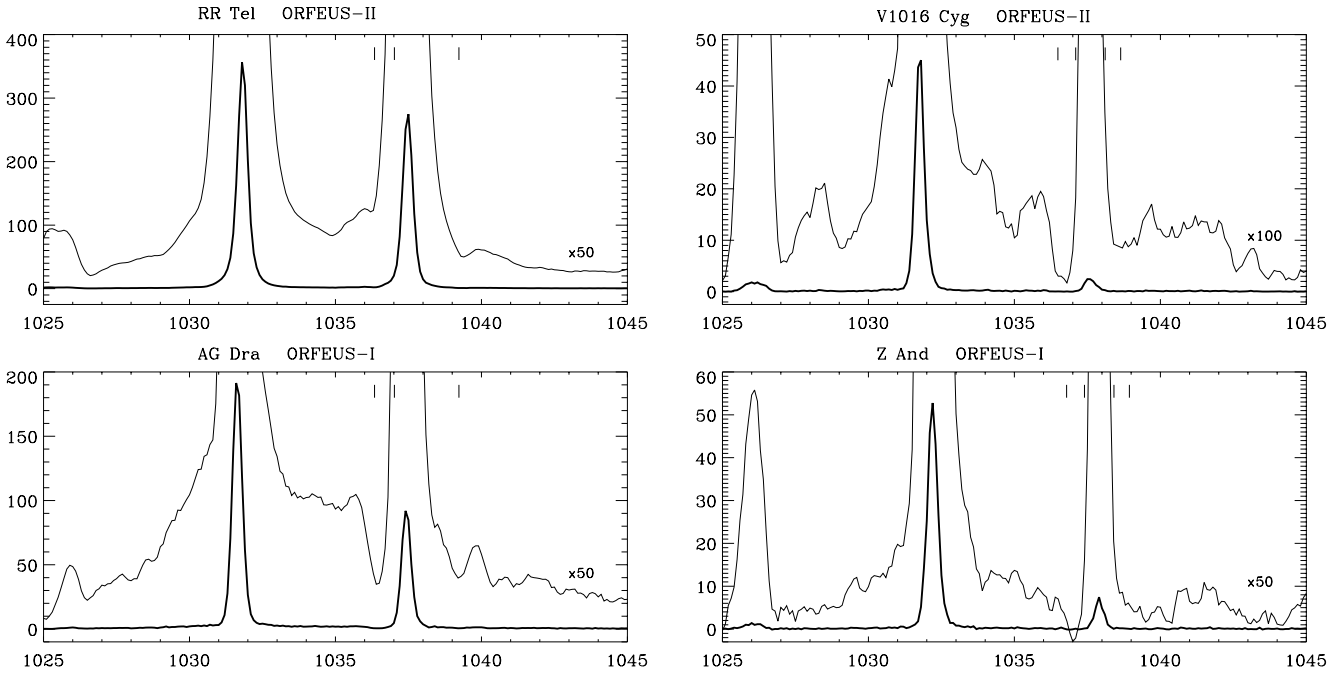

Fig. 1. Berkeley spectrograph O VI line profiles of RR Tel, V1016 Cyg, AG Dra and Z And. The flux scales correspond to the thick curve and are given in units of $10^{-12}\,\mathrm{erg\,cm^{-2}\,s^{-1}\,\AA^{-1}}$. Features in the weak line wings are illustrated by the thin curve which is the same spectrum multiplied by the factor indicated and smoothed with a boxcar of 5 pixels (0.5 Å). The short dashes give the expected location of strong interstellar lines due to C II and O I in RR Tel and AG Dra, and due to H_2 in V1016 Cyg and Z And. The feature near λ1026 is due to geocoronal Lyβ emission.

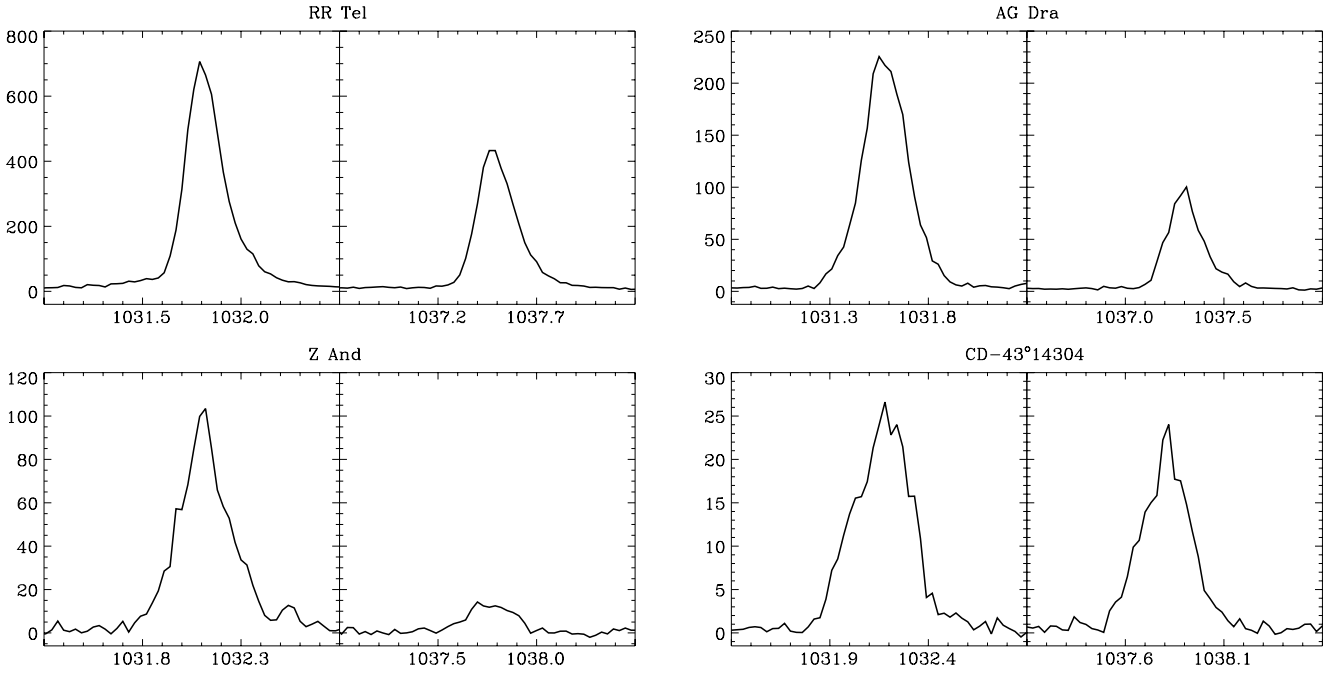

Fig. 2. ORFEUS-II Echelle spectrograph line profiles for the O VI doublets in RR Tel, AG Dra, Z And and CD$-43^\circ14304$. The wavelength scale has been corrected for pointing offsets. Fluxes are given in units of $10^{-12}\,\mathrm{erg\,cm^{-2}\,s^{-1}\,\AA^{-1}}$.

A detailed description of the Echelle spectrograph, its performance during the ORFEUS-II flight and the standard calibration of the data is given in Barnstedt et al. (1999). The achieved accuracy of the relative wavelength scale is better than 0.05 Å. However, for the absolute wavelength calibration there remains a wavelength uncertainty of at most ±0.12 Å for the O VI region, corresponding to a radial velocity uncertainty of ±36 km s^{-1}, caused by the unknown position of the target in the 20″-aperture.

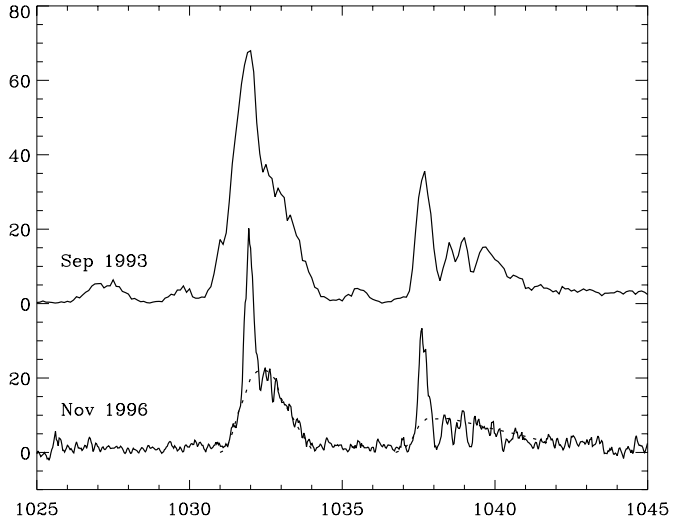

Fig. 3. O VI line spectra of AG Peg taken with the Berkeley spectrograph during the ORFEUS-I flight (top) and with the Echelle spectrograph during the ORFEUS-II mission (bottom). The Echelle spectrum has been slightly smoothed by a 3 pixel boxcar. The separation between the narrow nebular emission component and the broad wind emission component is indicated in the lower spectrum with a dotted curve. Fluxes are given in units of $10^{-12}\,\mathrm{erg\,cm^{-2}\,s^{-1}\,\AA^{-1}}$

It seems that our targets were all positioned near the edge of the aperture due to an off-center position of the fiducial point. This problem is addressed in the following section.

For the absolute flux calibration it must be considered that several targets were not well centered in the aperture. This problem is due to thermal drifts in the telescope alignment, which were larger than expected. It is in principle possible from the registered count rates to identify the time when the target was outside the aperture and correct the data accordingly. But this correction procedure is not applicable for the relatively faint symbiotic systems, because the count rates were strongly dominated by the background. As an alternative procedure, we compare the registered emission line flux in different exposures of the same target and reject those with strongly reduced flux. This assumes that at least one observation for a given target was not affected by light loss due to bad pointing. It is shown in the next section that the observations with good or bad pointing can also be recognized from the measured radial velocity shift in the spectrum.

2.3. Absolute wavelength calibration for the Echelle data

The spectra of the symbiotic systems contain several features which can be used as wavelength reference for an absolute wavelength calibration. We aim for an accuracy of ± 0.05 Å or ± 15 km s^{-1} in RV.

In AG Peg it is possible to measure accurately the position of the strong interstellar absorption lines due to H_2 and O I in the red wing of the O VI λ1038 emission line (see Fig. 3). For determining the RV of the interstellar lines we employ a high resolution $R = 50000$ optical spectrum of the Na I region around 5890 Å. This spectrum was taken with the ESO CAT 1.4m telescope within the framework of a high resolution study of symbiotic systems (e.g. Dumm et al. 1998). We find two narrow absorption components at -14 and $+3$ km s^{-1}. This result is supported by the HST GHRS spectrum of AG Peg (see Nussbaumer et al. 1995), where we measure a mean RV of -7 km s^{-1} for the S II λ1251 and λ1254 absorptions. Interstellar absorptions can also be recognized in the weak line wings of the O VI emissions in RR Tel, AG Dra and Z And. But due to the low signal these lines are not well enough defined for an accurate wavelength measurement. Nonetheless, we have used the interstellar absorptions for checking the absolute wavelength calibration for the individual spectra.

For RR Tel there exist HST GHRS spectra taken in July 1995 (see Nussbaumer & Dumm 1997), which cover partly the same wavelength range as our ORFEUS-II Echelle data. As RR Tel shows only very slow temporal changes in the emission lines, we can directly calibrate our spectrum to a very high accuracy.

For AG Dra, Z And and CD$-43°14304$ we use the nebular emission lines in the Echelle spectra, namely He II λ1084, O IV] λ1401 and for CD$-43°14304$ also O V] λ1218 as wavelength reference. The strong O VI and N V resonance lines are not used, because their central wavelengths are probably affected by a radiative transfer effect in a (slowly) expanding medium similar to P-Cygni lines.

We employed the strong He I emission line at λ7065 (also λ6678 and λ7281 for CD$-43°14304$), which were obtained simultaneously with our high resolution $R \gtrsim 10000$ observations of the Raman scattered O VI lines (see Sect. 9). The mean He I RV are -137 km s^{-1} for AG Dra, $+8$ km s^{-1} for Z And, and $+20$ km s^{-1} for CD$-43°14304$. AG Dra and Z And have been measured several times during three years without finding significant temporal changes beyond the measuring accuracy of about $\sigma_{\rm RV} \approx 5$ km s^{-1}. Further we note that our He I RV of AG Dra and Z And agree very well with previous measurements of Ivison et al. (1994). Our value for CD$-43°14304$ from 1996 differs also only slightly from the measurement of Van Winckel et al. (1993), who obtained $+30$ km s^{-1} in 1988.

Using the He I radial velocities (RV) for calibrating the far UV Echelle data assumes that the He I lines are emitted in a region with a very similar RV as the He II λ1084, the O IV] λ1401, or the O V] λ1218 lines. This is supported by high resolution studies of AG Dra, Z And and CD$-43°14304$, which obtained practically the same RV for the He II and the He I lines (Van Winckel et al. 1993; Ivison et al. 1994), or for high and lower excitation UV lines (Viotti et al. 1983).

Table 1 summarizes the correction procedure for the absolute wavelength or RV correction of the Echelle data. The correction for AG Peg based on interstellar lines and for RR Tel based on the HST spectra provide a high accuracy of ± 5 km s^{-1}. The indirect method via the RV of different emission lines contains potential uncertainties and limits the accuracy of the absolute calibration to about ± 15 km s^{-1}. All spectra have to be shifted to the red, indicating that the targets were all placed in the same corner of the aperture. The aperture size allows a pointing offset of at most ± 36 km s^{-1} in RV. Indeed, all spectra with reduced

Table 1. Radial velocity (RV) corrections applied to the Echelle spectra. Column 3 and 4 give the employed reference feature in the target spectrum and the adopted heliocentric radial velocity for these reference features. The next two columns give the applied radial velocity correction and the estimated error of the resulting RV calibration. The last column indicates whether the flux in the spectrum was low.

Object	date 1996	RV reference	RV adop.	RV cor.	RV err.	flux
AG Peg	11–23	IS abs.	-7	10	±5	
AG Dra	11–21	HeII, OIV	-137	30	±15	
	11–23	HeII, OIV	-137	43	±15	low
CD-43°	11–23	HeII, OIV/V	$+20$	40	±15	
14304	11–29	HeII, OIV/V	$+20$	46	±15	low
RR Tel	11–21	NV, Si/OIV	HST*	15	±5	
	11–29	NV, Si/OIV	HST*	30	±5	low
Z And	11–28	HeII, OIV	$+8$	36	±15	low
	12–01	HeII, OIV	$+8$	28	±15	

*: the RV correction was determined from the shift between HST and the ORFEUS Echelle spectra.

Table 2. Absolute line fluxes from the Berkeley spectra (in $10^{-12}\,\mathrm{erg\,cm^{-2}\,s^{-1}}$). The fluxes are not corrected for interstellar extinction.

Object	date	OVI 1032	OVI 1038	HeII 1085
AG Peg	93-09-16	95 ± 10	42 ± 5	19.5 ± 2.0
Z And	93-09-17	25 ± 1	2.5 ± 0.3	1.0 ± 0.1
AG Dra	93-09-18	95 ± 5	42 ± 4	5.1 ± 0.3
RR Tel	93-09-16	256 ± 5	154 ± 5	21.0 ± 1.5
	96-11-21	$196 \pm 5^*$	127 ± 5	14.0 ± 2.0
	96-11-23	$180 \pm 5^*$	135 ± 5	14.9 ± 2.0
	96-11-24	$179 \pm 5^*$	133 ± 5	14.6 ± 2.0
	96-11-25	$188 \pm 5^*$	135 ± 5	11.4 ± 2.0
	96-11-30	$154 \pm 5^*$	122 ± 5	15.6 ± 2.0
V1016 Cyg	96-11-30	19 ± 1	1.0 ± 0.1	1.2 ± 0.1

$*$: fluxes are too low by about 20% due to a saturation or spill over effect.

flux (see Table 1 and Sect. 3.2) have a RV offset of -30 km s^{-1} or more, indicating that the target was partly outside the aperture during the corresponding observation. The typical pointing jitter of the telescope, as measured with the star tracker, was only about $\pm2''$. Note that we allow RV corrections larger than 36 km s^{-1} which point to inaccuracies (within the expected errors) for the adopted systemic velocities.

3. O VI line fluxes

3.1. Line fluxes from the Berkeley spectra

Table 2 lists the O VI and He II line fluxes from the Berkeley spectra in absolute units. There are many more emission lines visible in the Berkeley spectra, especially for RR Tel (see e.g. Krautter et al. 1998). A discussion of these features is beyond the scope of this paper. The errors indicated in Table 2 represent only the uncertainties in the line flux measurements and neglect possible flux calibration problems.

In the flux measurements line wings are included and the continuum level was fixed by a linear fit to uncontaminated continuum regions on both sides of the line. However, it should be noted that the continuum is very weak in our objects. Therefore the definition of the continuum level is not critical for the fluxes of the strong emission lines given in Table 2 (see Fig. 1). Typical signal to noise ratios for the continuum in the Berkeley spectra are between $\mathrm{S/N} = 2$ and 6 except for the coadded RR Tel spectrum from the ORFEUS-II run, where the S/N-ratio is about 12.

A comparison with the Echelle spectra indicates that the extremely strong O VI λ1032 line in RR Tel measured during the ORFEUS-II flight, seems to have suffered from a slight saturation effect of about 20%. Apart from this line the five measurements of RR Tel made during the ORFEUS II flight agree well.

3.2. Line fluxes from the Echelle spectra

Relative line fluxes from the Echelle spectra are given in Table 3. This table includes besides O VI and He II λ1084, also the lines O V] λ1218 and N V $\lambda\lambda$1238,1242 longward of Lyα. Except for RR Tel, no other lines are strong enough for fluxes to be measured with reasonable accuracy. Relative line fluxes of a given object observed during different days of the ORFEUS II flight show no significant discrepancies above the expected measuring uncertainties of about 10% for strong lines and 20% for weak lines.

In the Echelle spectra practically no continuum radiation is visible. Thus, in Fig. 2 the scatter in the spectra near the plot boundaries gives an indication of the noise level.

Table 3 gives also the absolute flux for the two O VI lines based on the standard calibration procedure for the Echelle spectra. This assumes that the target was always well centered in the aperture. But several exposures have strongly reduced flux when compared with other exposures of the same target. These spectra exhibit also a large radial velocity offset $\Delta\mathrm{RV} \gtrsim 30$ km s^{-1} (see Table 1). Both findings indicate that the target was partly outside the aperture during the observation. The corresponding absolute O VI fluxes are therefore unreliable and put into brackets in Table 3. However, we find that the targets were well placed in the aperture for the Echelle spectra with high absolute O VI fluxes and small RV offsets. This is supported for RR Tel, AG Dra, AG Peg and Z And by a comparison with other far-UV measurements.

For RR Tel the absolute flux of the Echelle spectra from Nov. 21 is in very good agreement with the Berkeley spectra, except for the O VI λ1032 line. This line is about 20% stronger in the Echelle spectra, while the fluxes of the weaker O VI component at λ1038 match perfectly. The spill over effect described previously for the very strong O VI lines in the Berkeley spectra of RR Tel suggest saturation as cause for this discrepancy. Thus, we conclude that the O VI λ1032 line flux of RR Tel from the Berkeley data is too low by about 20% as indicated in Table 2.

Table 3. Line fluxes from the Echelle spectra. The columns 3 to 8 give fluxes relative to O VI λ1032, where $F(1032) = 100$. Columns 9 and 10 are the absolute fluxes of O VI λ1032 and λ1038 in $10^{-12}\,\mathrm{erg\,cm^{-2}\,s^{-1}}$ assuming that no light was lost due to bad pointing. The estimated uncertainty in the absolute O VI flux is given in the following column. For fluxes in brackets, it must be suspected that the source was outside the aperture for a significant fraction of the exposure time. The fluxes are not corrected for interstellar extinction.

Object	date	OVI		HeII	OV]	NV		F(OVI)	F(OVI)	error
		1032	1038	1085	1218	1238	1242	1032	1038	
AG Peg	96-11-23	100.	56.9			29.5	24.7	43.4	24.7	$+20\%/-10\%$
AG Dra	96-11-21	100.	33.2	4.0	3.0:	10.7	4.5	62.1	20.6	$+20\%/-10\%$
	96-11-23	100.	30.8	3.6	p	7.4	3.6	(45.0)	(13.9)	
CD$-43°14304$	96-11-23	100.	70.9	5.8:	20.4:	21.4	10.3	10.3	7.3	$+30\%/-10\%$
	96-11-29	100.	65.3	p	36.7:	p	p	(4.9)	(3.2)	
RR Tel	96-11-21	100.	60.5	5.0	4.4	21.2	11.7	218.	132.	$+10\%/-10\%$
	96-11-29	100.	55.8	4.5	4.5	22.7	10.3	(115.)	(64.0)	
Z And	96-11-28	100.	9.6	p	a	21.1	9.6	(15.6)	(1.5)	
	96-12-01	100.	11.8	p	a	18.3	9.9	35.5	4.2	$+20\%/-10\%$

p: present; a: absent; colon: larger uncertainty $> 20\%$ due to noise or strong geocoronal Lyα emission.

Far-UV line fluxes were measured for RR Tel and Z And with the Hopkins Ultraviolet Telescope (HUT) during the ASTRO-II space shuttle mission in March 1995 (Espey et al. 1995; Birriel et al. 1998). These measurements are in general agreement with the Echelle line fluxes when considering the expected variability of these objects (see next section).

For AG Dra, AG Peg and Z And the N V λ1238,1241 line fluxes measured with the Echelle spectrograph are in good agreement with previous IUE observations. This is shown in Fig. 4, where the N V doublet line fluxes are plotted as function of orbital phase. The IUE line fluxes were taken for AG Dra from Mikolajewska et al. (1995), and for Z And from Fernandez-Castro et al. (1995). For AG Peg we measured the N V line fluxes in the spectra available from the IUE archive. Fig. 4 includes only N V fluxes taken during the quiescent states of AG Dra and Z And. Similarly only fluxes taken between 1989–1995, after the strong stellar wind phase, were included for AG Peg (see e.g. Altamore & Cassatella 1997; Vogel & Nussbaumer 1994). References for the orbital ephemerides are given in Table 7. Phase 0 and 1 in Fig. 4 are the minima occurring when the cool giant is in front of the hot component.

We conclude that the absolute O VI fluxes given in Table 3 for AG Dra, AG Peg and Z And without brackets provide reliable measurements. Comparison with IUE data indicates that the possible loss should be less than $\lesssim 20\%$.

For CD$-43°14304$ there exists only one IUE spectrum, which was taken near the expected minimum phase (Schmid & Nussbaumer 1993; Schmid et al. 1998), and which is not helpful for checking the flux calibration. The quality of the telescope pointing for the ORFEUS observations of this object was certainly not very good, as we derived a large radial velocity correction of 40 ± 15 km s^{-1}, even for the spectrum with high flux. Therefore the absolute line fluxes for CD$-43°14304$ given in Table 3 could be underestimated by up to about 30%.

The O VI line flux ratios $F(\lambda1032)/F(\lambda1038)$ measured with ORFEUS (Tables. 2 and 3) differ from the theoretical value of 2 for an optically thin emission nebula. Substantially higher values are obtained for AG Dra, V1016 Cyg and Z And due to interstellar absorptions in the λ1038 component (see Sects. 4.5 and 5). Contrary to this, RR Tel and CD$-43°14304$ have an O VI line ratio below 2, which is not attributable to selective interstellar absorptions. However, such reduced line flux ratios are frequently observed in the ns–np resonance doublets of C IV,

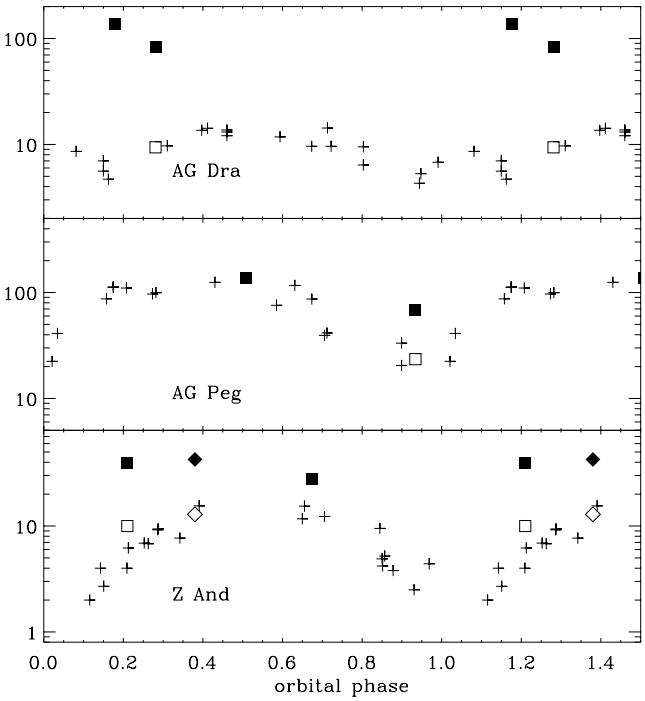

Fig. 4. N V $\lambda\lambda$1238,1242 and O VI $\lambda\lambda$1032,1038 line fluxes versus orbital phase for AG Dra, AG Peg and Z And (in quiescence). IUE data points for N V are given as crosses. Open symbols are N V fluxes and filled symbols O VI fluxes from the ORFEUS-I/II (squares) and ASTRO-II (diamonds) space shuttle missions.

N V, Mg II and Si IV in symbiotic systems. The physical nature of this "anomaly" is unclear (e.g. Michalitsianos et al. 1988).

3.3. O VI line flux variations

It is expected that the O VI line fluxes in symbiotic stars are variable on time scales of a few weeks or longer, similar to all other emission lines in these systems. The variations are mainly caused by the outburst activity of the hot component or by periodic obscuration due to the binary orbit. The O VI emission line variations could be comparable to those observed for the N V line (Fig. 4), because they have similar properties. Both the O VI and N V emissions are resonance doublets from highly ionized species. In addition, they have wavelengths close to a strong H I Lyman transition, where the Rayleigh scattering cross sections are large. Therefore a large fraction of emitted O VI and N V line photons undergo scattering in the neutral region around the cool giant (see e.g. Schmid 1995,1996).

AG Peg shows in our ORFEUS data a strong O VI line flux change of $F_{\rm Sep93}/F_{\rm Nov96} = 2.2$ between the first and second flight. This may be explained as orbital effect, as the high line flux from Sept 1993 was obtained very close to maximum phase at $\phi = 0.51$ and the low flux from Nov 1996 near minimum at $\phi = 0.93$ (see Fig. 4). The O VI maximum/minimum line flux ratio is smaller than the corresponding ratio $F_{\rm max}/F_{\rm min} \approx 4$ for the N V emission. The periodic N V line flux variations and the smaller changes in O VI are in qualitative agreement with model calculations, where the line radiation is mainly attenuated by H I Rayleigh scattering in the red giant's wind (see Schmid 1995,1996).

The O VI line fluxes of AG Dra and Z And changed roughly $\sim 40\%$ between Sep 1993 and Nov 1996. In addition there exists an O VI line flux measurement of Z And from the ASTRO-II mission (Birriel et al. 1998). The orbital phases of these observations are not as favourable as in AG Peg (see Fig. 4). Therefore no statement about phase-locked variations can be made. For AG Dra it should also be noted that the system underwent an outburst between the two observations (e.g. Greiner et al. 1997; Bastian 1998).

RR Tel shows a decrease in the O VI line flux of about 15% between Sep 1993 and Nov 1996. An additional O VI observation was made in March 1995 with HUT during the ASTRO-II mission (Espey et al. 1995). The measured flux for the entire O VI doublet $F = 387.4 \cdot 10^{-12}\,{\rm erg\,cm^{-2}\,s^{-1}}$ lies exactly between the ORFEUS-I and ORFEUS-II line fluxes. This indicates a steady decrease in the O VI line flux of RR Tel at least since 1993, in step with the observed overall fading of this symbiotic nova (Mürset & Nussbaumer 1994; Nussbaumer & Dumm 1997).

Most objects studied here were also observed between 1986 and 1991 with the VOYAGER-UVS instruments (Li & Leahy 1997). The measured line fluxes for RR Tel, AG Dra and AG Peg and the upper limit for Z And are within a factor of two in agreement with our measurements. Unfortunately the low sensitivity of the VOYAGER data allows no further statement about variability.

4. O VI line profiles

The ORFEUS telescope is the first instrument capable of measuring the line structure of the O VI lines in symbiotic systems. Therefore, we discuss in the following sections the observed O VI line profiles in detail. The two spectrometers of ORFEUS provide complementary information. The higher resolution of the Echelle data gives the structure and width of the narrow main component while the more sensitive Berkeley spectrometer reveals the spectral structures of the weak and broad line wings.

4.1. The narrow main component

A narrow nebular component dominates the O VI emission strongly in RR Tel, AG Dra, Z And, V1016 Cyg and CD$-43^\circ 14304$. The O VI line in AG Peg is composed of a narrow nebular line and a broad wind line. The O VI line centers and line widths as measured from the Echelle spectra are given in Table 4 in heliocentric radial velocities (RV). The values were determined by fitting a Gaussian profile to the measured line profiles. Using other techniques would alter the results by a few km s^{-1} at most, because the profiles are not strongly structured. The line widths of the nebular O VI component in AG Peg depends also somewhat on the adopted profile for the wind component.

The central RV of the O VI lines in our symbiotic systems are shifted by about 20–60 km s^{-1} to the red with respect to the systemic RV, and a similar shift relative to the optically thin intercombination lines. This behaviour can be explained as a line absorption/scattering effect in an expanding medium (see next section). For the systemic RV we adopted for AG Dra, CD$-43^\circ 14304$, AG Peg and Z And the values from the RV curves of the cool component (Mikolajewska et al. 1995; Smith et al. 1996; Schmid et al. 1998; Kenyon et al. 1993; Mikolajewska & Kenyon 1996), and for RR Tel the mean RV of the nebular emission lines (Thackeray 1977).

The O VI line widths are given in Table 4. The widths are corrected for the limited resolution of the instrument. The intrinsic O VI line widths $\Delta{\rm RV}_{\rm intr}$ are about 5–15% smaller than the observed line widths $\Delta{\rm RV}_{\rm obs}$. This estimate follows from the instrument resolution of $\Delta{\rm RV}_{\rm res} = 30$ km s^{-1} and the formula $\Delta{\rm RV}_{\rm intr} = (\Delta{\rm RV}^2_{\rm obs} - \Delta{\rm RV}^2_{\rm res})^{1/2}$, which adopts a simplified description of the instrument broadening as convolution of a Gaussian line with a Gaussian instrument profile.

The line widths and/or central radial velocites ${\rm RV}_c$ of the two O VI lines λ1032 and λ1038 show in AG Dra, CD$-43^\circ 14304$ and Z And substantial differences > 10 km s^{-1}. These differences are mainly produced by strong interstellar absorptions in the λ1038 component (see Sect. 4.5).

Asymmetric line profiles are clearly seen in both O VI lines in RR Tel. Both components show a steeper blue side and an extended wing on the red side. In AG Dra, Z And and CD$-43^\circ 14304$ the O VI λ1032 line does not differ strongly from a Gaussian line.

Table 4. Line center and width for the O VI lines derived from the Echelle spectra. The values are given as radial velocities (RV) in units of km s^{-1}. The line widths are corrected for instrumental broadening.

	AG Dra		RR Tel		CD−43°14304		AG Peg^{+}		Z And	
	λ1032	λ1038	λ1032	λ1038	λ1032	λ1038	λ1032	λ1038	λ1032	λ1038
					line center*					
heliocentric	−99	−93	−35	−40	+68	+49	+13	+7	+55	+41
intrinsic	+49	+55	+27	+22	+40	+21	+29	+23	+57	+43
adopted system RV	−148		−62		+28		−16		−2	
					line width (FWHM)					
	71	51	55	55	93	76	$\sim 95^{+}$	$\sim 95^{+}$	78	71

$*$: adopted O VI rest wavelengths are 1031.926 Å and 1037.617 Å; $+$: nebular line component only; the line width of the nebular component in AG Peg depends on the adopted wind line structure (the estimated uncertainty in FWHM is 15%)

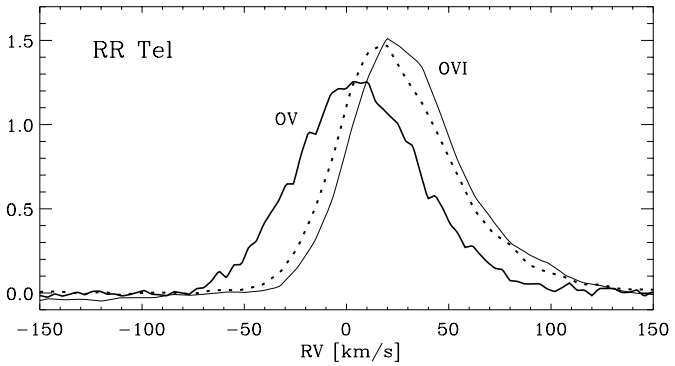

Fig. 5. O VI line transfer effect in RR Tel: The O VI λ1032 (solid) and λ1038 (dotted) resonance lines are displaced relative to the optically thin recombination line of O V λ1643 (thick line). RV $= 0$ km s^{-1} corresponds to the adopted systemic radial velocity of -62 km s^{-1}. All profiles are normalized to the same total line flux.

4.2. Line transfer effect in the O VI lines

The systematic redshift of the O VI resonance lines with respect to the system velocity can be explained as radiative line transfer effect in an expanding medium. Fig. 5 illustrates this for RR Tel, where the structure of the optically thin O V λ1643 recombination line is compared to the O VI resonance lines. The O V λ1643 line was taken with the Hubble Space Telescope (HST) and GHRS in July 1995 (see Nussbaumer & Dumm 1997). Because RR Tel shows practically no spectral changes, the line profile differences between O V and O VI are certainly not a variability effect. In fact, the comparison of the O VI lines with the simultaneously observed O V recombination line at λ1371 in the ORFEUS Echelle spectrum shows exactly the same effect, although the O V line is very noisy.

The O V recombination line is formed in the same nebular region as the O VI resonance lines, namely the O^{+5}-region. Comparison between these lines gives therefore a good indication of the size of the radiative transfer effect in the O VI resonance lines. Interestingly the λ1038 component shows a smaller redshift. This is naturally explained by the smaller oscillator strength of this transition, and the correspondingly smaller optical depth.

The scattering of line photons in an expanding medium is an attractive explanation for the observed O VI line structure. The high densities and the narrow line widths observed for the emission nebula in symbiotic systems are ideal for producing such an line absorption/scattering effect. The interpretation is also strongly supported by the study of Friedjung et al. (1983), who found the same effect in the C IV, N V and Si IV resonance lines of many symbiotic systems.

4.3. The wind lines in AG Peg

The O VI emission lines of AG Peg display broad wind lines as expected from a fast stellar wind outflow for both the 1993 and the 1996 observation (Fig. 3). A dotted line is shown in the Nov. 1996 spectrum, which separates tentatively the narrow nebular emission from the broad wind component. According to this separation 70 ± 5% of the total line flux is due to the broad wind emission in both O VI lines. The wind emission of the λ1038 components longwards of the narrow nebular component extends to about +3.5 Å from the rest wavelength or to a radial velocity (RV) of $+1000$ km s^{-1}. The red line wing of the λ1032 component is narrower with an extension of only about +2.3 Å. This coincides with the expected edge of a -1000 km s^{-1} wide absorption trough of a P-Cygni line profile from the λ1038 component.

This type of broad stellar wind profiles has been observed previously in AG Peg for the C IV and N V resonance lines in (e.g. Penston & Allen 1985; Kenyon et al. 1993; Vogel & Nussbaumer 1994; Nussbaumer et al. 1995; Altamore & Cassatella 1997). The strengths of the C IV and N V wind components decreased strongly in the eighties while the narrow nebular emission became dominant. The same may occur currently with the O VI wind lines. Interestingly the width of the wind lines which reflects the outflow velocity remained roughly constant since 1970 at $\approx$ 700–950 km s^{-1}. Even the mass loss rate remained at about the same level, so that the observed wind line changes are mainly due to an increase of the ionization degree in the stel-

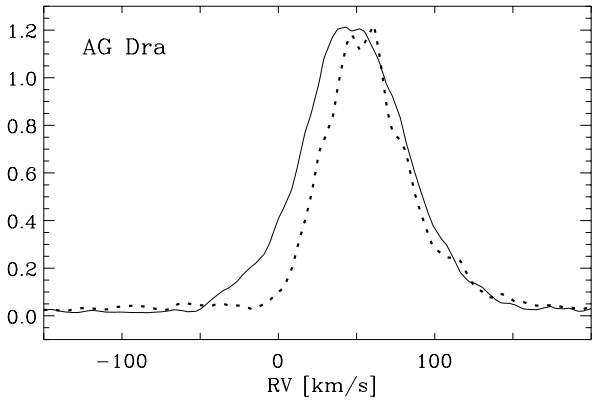

Fig. 6. Comparison of the O VI λ1032 (solid) and λ1038 (dotted) line structures in AG Dra. The profile difference is mainly caused by interstellar C II λ1037.02 absorption in the blue wing of the λ1038 component. The two O VI lines are scaled to the same peak flux.

lar wind as result of the temperature evolution of the underlying star (Schmutz 1996).

4.4. Broad, weak line wings

Weak, broad line wings are observed for the O VI lines in AG Dra, RR Tel and V1016 Cyg (see Fig. 1). These wings extend in all three objects from approximatelly 1026 Å to 1044 Å. Strong interstellar absorptions in these line wings confirm that they are mainly intrinsic to the symbiotic systems and not caused by a light scattering effect in the spectrograph.

The broad features could be interpreted as a superposition of two pairs of line wings centered at the position of the two narrow O VI lines, and having a width (FWHM) of 5–6 Å or a RV-width of roughly 1600 km s^{-1}. An attractive explanation for these line wings is scattering of O VI line photons by electrons. The widths of the wings require a kinetic temperature for the electrons of about 30000 K. Such temperatures are derived for the highly ionized nebular regions of symbiotic systems (e.g. Schmid & Schild 1990). Similar 'electron scattering' wings in strong UV emission lines have already been observed in other spectra of symbiotic systems (e.g. Viotti et al. 1983; Schmutz 1996).

4.5. Interstellar absorptions

As mentioned in previous sections the O VI line fluxes and profiles, especially of the λ1038 component, can be significantly affected by interstellar absorptions. Many strong interstellar absorptions are expected near the O VI λ1038 line, namely the first transitions from the Lyman 5–0 band of molecular hydrogen at $\lambda\lambda$1036.54, 1037.15, 1038.16, 1038.69, 1040.37 and the strong atomic absorptions from C II $\lambda\lambda$1036.34,1037.02 and O I λ1039.23 (see e.g. Morton 1975).

The Echelle spectra have not enough flux to see interstellar absorptions, except where they coincide with strong emission lines. As a result of such absorptions in the steep line flanks we see in AG Dra, CD-43°14304 and Z And λ1038 emission lines, which are shifted in RV or which are narrower when compared to the λ1032 line (see Fig. 6). But this information is not sufficient to identify unambiguously the absorbing line transition. Fortunately, the more sensitive Berkeley spectrograph recorded a weak far-UV continuum for RR Tel, AG Peg, AG Dra, Z And and V1016 Cyg, where many interstellar absorptions can be recognized. In Fig. 1 some interstellar absoptions near the O VI λ1038 line are indicated.

Strong H_2 absorption bands are seen in V1016 Cyg, Z And and AG Peg as expected from cool molecular clouds. For Z And and V1016 Cyg the H_2 absorptions are particularly strong and attenuate significantly the O VI λ1038 component. The measured doublet ratio is $F(\lambda1032)/F(\lambda1038) \approx 10$ in Z And and ≈ 18 in V1016 Cyg; much larger than the expected theoretical value of two. Therefore, it is expected that the structure of the observable O VI λ1038 line differs significantly from the intrinsic line structure in these objects. This effect is modelled and discussed in more detail in the next section.

The H_2 lines are weak or absent in the FUV continuum of RR Tel and AG Dra. This is not surprising as both objects are located at high galactic latitudes. From this, we can also conclude that the important interstellar absorptions in the O VI λ1038 region originate from C II and O I. Signatures of the C II $\lambda\lambda$ 1036,1037 lines in the blue line wing of O VI λ1038 are indeed visible in the spectra of AG Dra and RR Tel.

5. Modelling the H_2 absorptions in the O VI lines

The flux of O VI λ1038 in V1016 Cyg and Z And is strongly reduced when compared to the line at λ1032 line. Observations of interstellar absorptions (e.g. Morton 1975) suggest that the λ1038 line is reduced due to absorption in the damping wings of strong H_2 transitions. This interpretation is supported by the fact that the Echelle spectrum of Z And (see Fig. 2) shows no narrow absorption components in the λ1038 component. As we are interested in the intrinsic O VI line flux, we investigate in this section the attenuation of the O VI lines by interstellar H_2 and H I. Thereby only a general assessment of the effects is given. It is not possible to make meaningful spectral fits to the interstellar absorptions in our spectra, because the signal in the continuum is too low. Fitting line absorptions in the strong, narrow emission lines would require data with higher spectral resolution. Nontheless, it is possible to define a criterion indicating the cases where absorptions by interstellar lines are negligible for the O VI λ1032 emission.

We have constructed a model for the interstellar H_2 and H I Lyβ absorptions. The H_2 absorption model is based on the wavelengths and oscillator strengths from Abgrall et al. (1993a,b) kindly provided by Dr. E. Roueff in computer readable form. Out of the about 26 000 lines we preselected the transitions from the electronic and vibrational $\nu'' = 0$ ground state of the Lyman band system with $J'' = 0$–10 and wavelengths 1020 Å $< \lambda < 1050$ Å. The radiative damping constants for calculating the natural broadening of the absorption lines were taken from Morton & Dinerstein (1976). The population of the rotational levels J'' was assumed to be in a thermal equilib-

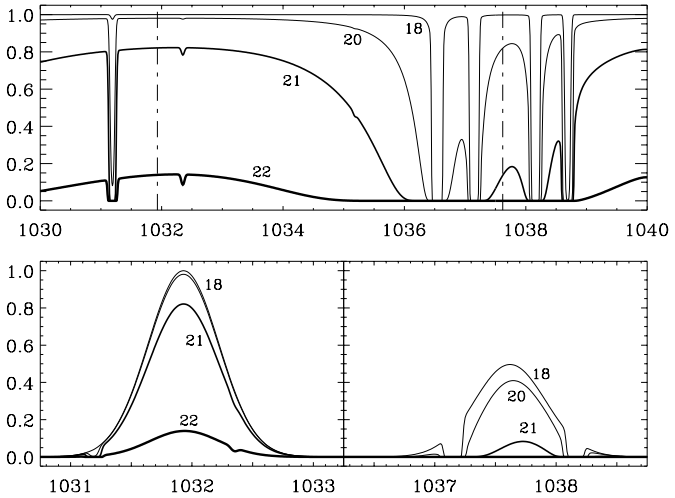

Fig. 7. The upper panel shows the calculated transmission functions between 1030 Å and 1040 Å for the interstellar H_2 column densities in cm^{-2} $\log(d_{\mathrm{H2}}) = 18$, 20, 21, and 22. The positions of the O VI transitions are indicated with dashed-dotted lines. The lower panel illustrates the impact of this absorption on Gaussian O VI line profiles with a $\mathrm{FWHM} = 200\ \mathrm{km\,s^{-1}}$.

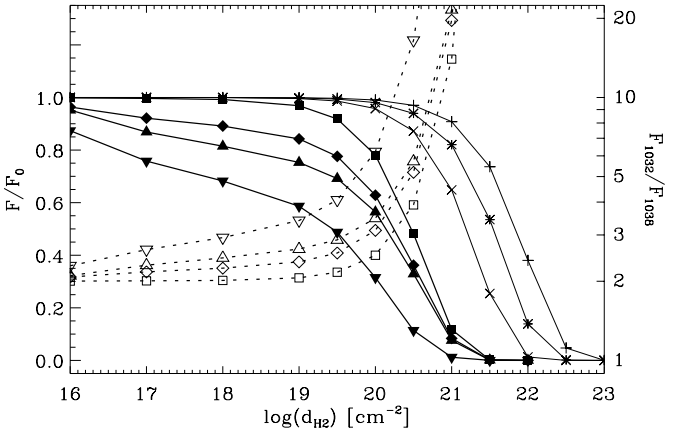

Fig. 8. Interstellar transmission function F/F_0 for O VI λ1032 and λ1038 (left axis) and the line ratio $F(1032)/F(1038)$ (right axis) as function of the H_2 column density $\log d_{\mathrm{H2}}$ [cm^{-2}]. F/F_0 for λ1032 is given with thin solid lines for the abundance ratios $Q_{\mathrm{H/H2}} = 0$ (+), 3 (∗), and 10 (×). Thick solid lines and filled symbols are used for the λ1038 component with different radial velocity shifts / line widths (FWHM) given in $\mathrm{km\,s^{-1}}$. The symbols stand for 0/100 (boxes), 0/200 (diamonds), +100/100 (upward triangles), and –100/100 (downward traingles). The resulting line ratios $F(1032)/F(1038)$ are given as dotted lines assuming an initial line ratio of $F_0(1032)/F_0(1038) = 2$ The open symbols for the line ratios correspond to the filled symbols for the used λ1038 F/F_0 curves. All line ratios were calculated using for λ1032 the abundance ratio $Q_{\mathrm{H/H2}} = 3$.

rium defined by an excitation temperature T_{H2}. In addition we consider the absorption due to the H I Lyβ transition.

Model parameters are the column density for molecular hydrogen d_{H2}, the Doppler velocity parameter b for describing the velocity distribution of the absorbing particles along the line of sight, the H_2 excitation temperature T_{H2}, and the number abundance ratio between atomic and molecular hydrogen $Q_{\mathrm{H/H2}} = N(\mathrm{H\,I})/N(\mathrm{H_2})$. Optical depths were calculated using Voigt profiles at 0.01 Å intervals.

The following model is only representative for absorptions in a cool molecular cloud. Absorptions from higher H_2-transitions are expected from the hot intercloud medium and even O VI resonance absorptions may be present from highly excited interstellar regions. Such absorption lines are neglected here, because they are expected to be much weaker than the H_2 lines from cool molecular clouds.

Fig. 7 shows the transmission function near the O VI lines for the column densities $d_{\mathrm{H2}} = 10^{18}$, 10^{20}, 10^{21}, and $10^{22}\,\mathrm{cm}^{-2}$. For the other parameters the values $b = 10\ \mathrm{km\,s^{-1}}$, $T_{\mathrm{H2}} = 100$ K, and $Q_{\mathrm{H/H2}} = 3$ were adopted. It is assumed that both, the interstellar absorptions and the O VI emissions, are at their rest wavelengths. The computed transmission spectra illustrate that the line damping wings become substantial for column densities of $d_{\mathrm{H2}} \gtrsim 10^{20}\,\mathrm{cm}^{-2}$ at the position of the λ1038. Ten times higher column densities are required for substantial reduction of the λ1032 component.

The impact of the interstellar absorptions on the O VI emission line structures is illustrated in the lower panels of Fig. 7. There, the interstellar transmission function is multiplied with Gaussian line profiles at the O VI rest wavelenghts and a FWHM of 200 $\mathrm{km\,s^{-1}}$ or 0.69 Å. The Gaussian profiles were normalized to the peak intensities $F_p(1032) = 1$ and $F_p(1038) = 0.5$. For all curves a H_2-excitation temperature of $T_{\mathrm{H2}} = 100$ K and a Doppler spread of $b = 10\ \mathrm{km\,s^{-1}}$ was adopted.

For the O VI λ1038 component strong narrow absorptions of H_2 are seen in Fig. 7 in the line wings for column densities as low as $d_{\mathrm{H2}} = 10^{18}\,\mathrm{cm}^{-2}$. The narrow absorptions reduce the O VI λ1038 line flux less than $\lesssim 15\%$ unless the O VI line is shifted significantly in radial velocity by $\pm 100\ \mathrm{km\,s^{-1}}$ or more relative to the interstellar absorptions. For higher column densities the entire blue wing of the λ1038 component is attenuated by the strong H_2 5–0 R(1) transition at λ1037.15 and the red wing is strongly affected by the 5–0 P(1) transition at λ1038.16. The resulting profile is determined by the overlapping damping wings of the interstellar lines and the remaining λ1038 emission is shifted to the red. It should be noted that the O VI line widths in symbiotic systems are typically 50–100 $\mathrm{km\,s^{-1}}$, much narrower than plotted in Fig. 7. The large line width in Fig. 7 was chosen in order to illustrate the narrow H_2 absorptions in the line wings, which would be hardly visible for a narrower (unshifted) O VI λ1038 emission.

The spectral region around the O VI λ1032 component is free of strong H_2-absorptions. For very high column densities ($d_{\mathrm{H2}} \gtrsim 10^{21}\,\mathrm{cm}^{-2}$), the flux of the O VI λ1032 line is strongly attenuated by the damping wings of the H_2 6–0 transitions near λ1025 and the H I Lyβ line. Therefore the transmitted flux depends on the adopted $Q_{\mathrm{H/H2}}$ ratio, but not on radial velocity shifts or emission line width. Very helpful for the analysis of the O VI line structures is that the line structure of the λ1032

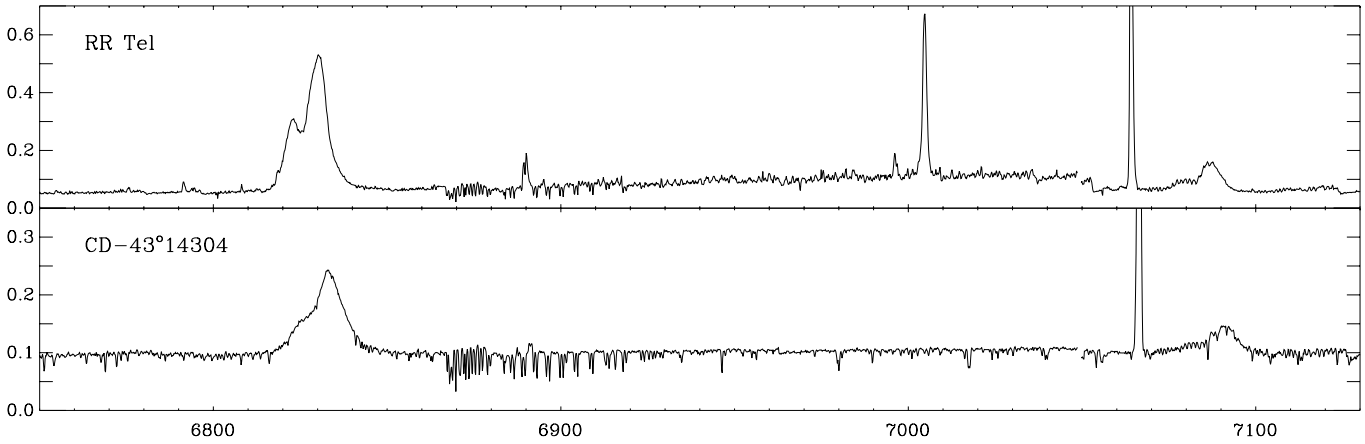

Fig. 9. RR Tel and CD$-43^\circ 14304$ high resolution spectra (ESO 3.6m, CASPEC) of the spectral region near the broad Raman scattered O VI lines at λ6825 and λ7082. Strong narrow emission lines are due to [Ar V] λ7005 (only RR Tel) and He I λ7065. The flux is given in $10^{-12}\,\mathrm{erg\,cm^{-2}\,s^{-1}\AA^{-1}}$.

component is practically not changed by the absorption in the damping wings.

The corresponding effect on the integrated O VI line fluxes as a function of column density is shown in Fig. 8. The line ratios $F(\lambda1032)/F(\lambda1038)$ are plotted as dotted lines. For this ratio it is assumed that the initial line ratio is $F_0(1032)/F_0(1038) = 2$, as expected for an optically thin emission nebula. The transmitted O VI line ratio is strongly enhanced for column densities $d_{\rm H2} > 3 \times 10^{20}\,\mathrm{cm^{-2}}$ due to absorption of the λ1038 component. The important result from Fig. 8 is that the strength of the interstellar absorptions in the O VI λ1032 emission can be estimated from the observed O VI line ratio. It can be concluded that interstellar absorptions are relatively small for the O VI λ1032 component and can be neglected for our purposes as long as the line ratio is $F(\lambda1032)/F(\lambda1038) < 20$.

6. Observations of the Raman scattered O VI lines

Spectroscopic observations of the Raman lines of the two southern objects RR Tel and CD$-43^\circ 14304$ have been obtained with ESO telescopes at La Silla. The northern objects AG Dra, Z And, AG Peg and V1016 Cyg are frequently observed objects and their Raman line fluxes and profiles were taken from the literature or from the spectropolarimetric monitoring program described in Schild & Schmid (1996,1997) and Schmid & Schild (1997a,b).

6.1. ESO observations

Spectrophotometric observations of RR Tel have been taken just two months after the ORFEUS-I observations during the nights of November 21–23, 1993 with EFOSC1, a focal reducer spectrograph/camera, attached to the ESO 3.6m telescope. Intermediate resolution spectra $\Delta\lambda \approx 4$ Å were taken in the Echelle mode of EFOSC. For the flux calibration of the echelle data, low resolution spectra $\Delta\lambda \approx 15$ Å were taken on November 23, 1993 under photometric conditions with the B300 and R300 grism and a 5″-wide aperture slit. The observational details are identical to the data described in Mürset et al. (1996).

Low and high resolution spectra of RR Tel and CD$-43^\circ 14304$ were obtained with the ESO-telescopes in October 1996, only about 7 weeks before the ORFEUS-II flight. Low resolution spectrophotometric data were taken on October 8, 1996 under photometric conditions with EFOSC2 at the 2.2m telescope. The employed slit width of 5″ together with the B1000 grism and CCD (#40) gave a spectral resolution of about 40 Å and a wavelength coverage from about 3300 Å to 9900 Å. The spectra were flux calibrated by comparison with the standard star Feige 110. These data were used to flux calibrate the high resolution spectra of RR Tel from October 8, 1996 and CD$-43^\circ 14304$ from October 7, 1996 taken with CASPEC on the 3.6m telescope. CASPEC is a cassegrain echelle spectrograph which was employed with the red cross disperser and a Tek 1k×1k CCD (#37). The obtained resolution is about $R = 20000$ and the wavelength coverage is from 6100 Å to 7400 Å. The accuracy of the wavelength calibration for the CASPEC spectra is ≈ 0.05 Å (≈ 2 km s^{-1}).

All data were reduced with the MIDAS packages for long slit and echelle spectroscopy. Table 5 gives the measured line fluxes for the Raman scattered O VI lines together with some other strong or interesting lines. We estimate an accuracy of about 30% for the line fluxes in Table 5. A portion of the CASPEC high resolution spectra including the Raman scattered O VI lines are plotted in Fig. 9.

7. Raman line fluxes

We summarize here the spectroscopic information collected from various sources in order to estimate the line flux of the Raman scattered emission lines at the time of the far-UV ORFEUS-I and ORFEUS-II observations. Because there often do not exist simultaneous measurements we consider the long term behaviour of the emission line spectra and try to interpolate or extrapolate between existing data. Each object is discussed individually in

Table 5. Line fluxes for RR Tel and CD−43°14304 (in $10^{-12}\,\mathrm{erg\,cm^{-2}\,s^{-1}}$) measured with ESO telescopes.

line	RR Tel		CD−43°14304
	Nov. 93	Oct. 96	Oct. 1996
4340 Hγ	9.3	}18.2	2.9
4363 [O III]	6.3		···
4686 He II	21.2	21.7	3.1
4861 Hβ	23.0	22.6	7.9
4959 [O III]	14.1	}46.2	···
5007 [O III]	36.1		···
5876 HeI	1.7	···	0.9
6087 [Fe VII],[CaV]	16.0	13.6	···
6563 Hα	85.8	74.9	27.6
6678 HeI	1.1	0.47	0.36
6683 HeII*	···	0.17	0.013
6825 Raman line	7.2	4.5	1.7
7065 HeI	2.0	1.35	0.76
7082 Raman line	1.2	0.91	0.6

···: too weak; ∗: He II line used for reddening determination

the following sections. The adopted λ6825 and λ7082 line fluxes are given in Table 7.

For the line flux measurements the stellar and nebular continuum was subtracted. Depending on the strength of the underlying stellar absorptions this was done with a linear, local continuum fit (e.g. for λ6825 in RR Tel) or an appropriate stellar absorption spectrum (e.g. for λ7082).

7.1. Z And

Z And was in quiescent state from 1988 to 1997 which includes both our ORFEUS observations. Mikolajewska & Kenyon (1996) observed the λ6825 Raman line five times during the 1994/1995 season and obtained a mean flux of about $4.5 \cdot 10^{-12}\,\mathrm{erg\,cm^{-2}\,s^{-1}}$ with a scatter of $\pm 15\%$. The relatively small line flux variations are in agreement with the equivalent width measurements of Schmid & Schild (1997b), which cover the period from Aug. 1991 to Oct. 1994. One measurement in this series was taken just 26 days prior to the ORFEUS-I measurement. No Raman line flux measurements were published for dates after Feb. 1995.

For both the ORFEUS-I and ORFEUS-II observations we adopt the mean value $F(\lambda 6826)$ given above. We adopt an uncertainty of $\pm 15\%$ for the ORFEUS-I run and due to the lack of contemporary measurements $\pm 30\%$ for the ORFEUS-II run. The line flux of the λ7082 line in Table 7 follows from the line flux ratio $F(\lambda 6825)/F(\lambda 7082) = 3.6$ determined by Schmid & Schild (1997b).

7.2. AG Dra

The Raman line fluxes for AG Dra were studied in some detail in Schmid & Schild (1997a). It was found that they show no regular trend over longer time scales. The existing observations suggest that the line strength of λ6825 remains around $7 \pm 4 \cdot 10^{-12}\,\mathrm{erg\,cm^{-2}\,s^{-1}}$. Orbital effects seem to be unimportant and unlike most other emission lines the Raman line fluxes are not strongly enhanced during outbursts (see Mikolajewska et al. 1995; Iijima et al. 1987).

The ORFEUS-I observations of AG Dra were taken during a quiescence state. Schmid & Schild (1997a) determined a λ6825 line flux of $10.5 \cdot 10^{-12}\,\mathrm{erg\,cm^{-2}\,s^{-1}}$ for August 22, 1993 just 26 days before the ORFEUS-I run. We adopt this value and an uncertainty of 25% for the ORFEUS-I run. The ORFEUS-II observation were taken at the end of an outburst episode. At the moment no λ6825 flux measurements are available near this run and we adopt the long term mean line flux. The measured line ratio $F(\lambda 6825)/F(\lambda 7082) = 2.4$ (Schmid & Schild 1997a) gives the flux of the weaker component at λ7082.

7.3. RR Tel

The line fluxes measured at ESO for RR Tel were taken near the ORFEUS-I and ORFEUS-II observations. RR Tel shows only slow variations in the emission line fluxes (e.g. Hayes & Nussbaumer 1986; Aufdenberg 1993; Nussbaumer & Dumm 1997). Therefore, we can adopt the fluxes in Table 5 for the corresponding ORFEUS observations.

The flux of the Raman lines has also been determined for May 18, 1995 shortly after the ASTRO-II observations (see Espey et al. 1995). The measured λ6825 flux for that date is $5.6 \pm 0.8 \cdot 10^{-12}\,\mathrm{erg\,cm^{-2}\,s^{-1}}$ which lies between our 1993 and 1996 fluxes. Thus the flux of the Raman scattered lines decreases steadily as for the far-UV O VI emission lines.

7.4. V1016 Cyg

V1016 Cyg was slowly evolving up to 1985 in the sense that the high excitation emission lines became stronger and the low excitation lines stayed constant or weakened slightly (Nussbaumer & Schild 1981; Schmid 1990; Schmid & Schild 1990; Mürset & Nussbaumer 1994). Since 1985 no significant line flux changes have been reported. The Raman line fluxes $F(\lambda 6825) = 4.4 \cdot 10^{-12}\,\mathrm{erg\,cm^{-2}\,s^{-1}}$ and $F(\lambda 7082) = 0.62 \cdot 10^{-12}\,\mathrm{erg\,cm^{-2}\,s^{-1}}$ were measured in November 1987 by Schmid & Schild (1990). About a year later Rudy et al. (1990) obtained a λ6825 flux, which is about 40% lower. Because the relative line fluxes of Schmid & Schild (1990) and Rudy et al. (1990) agree very well, we must conclude that the discrepancy comes from the absolute flux calibration. In the following we adopt for V1016 Cyg the mean value $F(\lambda 6825) = 3.5 \pm 1 \cdot 10^{-12}\,\mathrm{erg\,cm^{-2}\,s^{-1}}$ and a correspondingly scaled value for $F(\lambda 7082)$. We are not aware of Raman line fluxes measurements since then. However, spectropolarimetric data taken between 1991 and 1997 suggest no or only little variability in the line fluxes (see Schild & Schmid 1996).

7.5. CD−43°14304

Our Raman line fluxes for CD−43°14304 (Table 5) were measured about 50 days before the ORFEUS-II observations. Equiv-

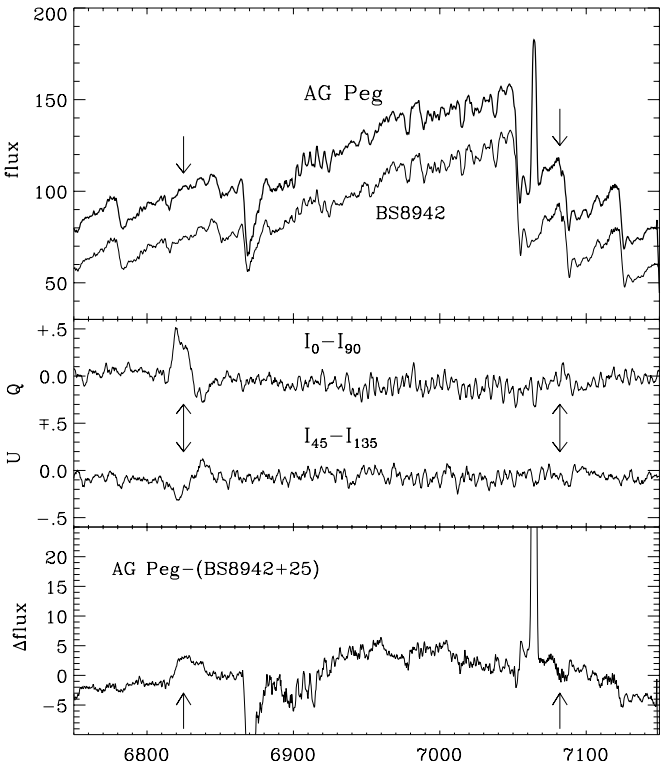

Fig. 10. Red spectrum of AG Peg. Top: Intensity spectra of AG Peg and the M3 III giant BS 8942. Center: Stokes Q and U spectrum for AG Peg showing a polarization signal at the positions of the Raman lines. Bottom: difference spectrum of AG Peg and BS 8942 (+ constant) which reveals the weak λ6825 feature in AG Peg. The arrows indicate the expected position λ6825 and λ7082 of the O VI Raman lines. All spectra are plotted on the same relative flux scale where 100 corresponds to $0.75 \cdot 10^6$counts/pixel.

alent width measurements of the λ6825 line indicate only slow line flux variations on time scales of several hundred days which are probably locked to the $P = 1448$ day orbit of the system (Schmid et al. 1998). Therefore it seems safe to adopt the ESO values for the ORFEUS-II run.

7.6. AG Peg

In AG Peg, the Raman scattered O VI lines have not been detected previously. Kenyon et al. (1993) estimated an upper limit for the λ6825 line flux of $F < 2.0 \cdot 10^{-12}\,\mathrm{erg\,cm^{-2}\,s^{-1}}$. As the ORFEUS-II run confirmed the earlier detection of strong O VI emission lines in the far-UV, we searched on June 26, 1997 spectropolarimetrically for the Raman scattered counterparts with the WHT. The instrumentation and reduction for these data is very similar to those described in e.g. Schild & Schmid (1996). The resulting spectra are plotted in Fig. 10 with a 11-pixel boxcar smoothing, where 1 pixel corresponds to 0.3 Å.

A clear polarimetric signal of the λ6825 component was detected as shown in Fig. 10. A trace of the same spectropolarimetric signature can also be seen at the position of the weaker component around λ7082. The subtraction of a spectrum of the M3 III giant BS 8942 reveals also the intensity spectrum of the λ6825 line. The λ7082 intensity component is not visible in the difference spectrum. This can be explained partly because the λ7082 line is weaker, and partly because the stellar spectrum is very strongly structured around this wavelength so that the applied subtraction procedure is not accurate enough.

From the λ6825 line intensity in the residual spectrum an emission line equivalent width of 0.70 ± 0.20 Å is derived. According to Fig. 1 in Kenyon et al. (1993) and considering the long term photometric evolution of AG Peg, a continuum flux of $2 \cdot 10^{-12}\,\mathrm{erg\,cm^{-2}\,s^{-1}\AA^{-1}}$ is estimated around 6800 Å. The obtained line flux of $F = 1.4 \pm 0.7 \cdot 10^{-12}\,\mathrm{erg\,cm^{-2}\,s^{-1}}$ is consistent with the upper limit derived by Kenyon et al. (1993).

The width of the detected λ6825 component in AG Peg is about 18 Å in both the intensity and the polarization spectrum. This is the expected width for the Raman scattered counterparts of the narrow nebular component observed in the far-UV. No signatures of Raman scattered radiation from the broad stellar wind lines are seen, which are expected between 6850 Å and 6950 Å or between 7100 Å and 7200 Å. However, it should be noted that a 100 Å broad and little structured Raman scattering feature is hard to detect, if its integrated intensity or polarization is substantially smaller than for the narrow component at λ6825.

8. Raman scattering efficiency

The Raman scattering efficiency is defined as the photon ratio $N_{\mathrm{Raman}}/N_{\mathrm{O\,VI}}$ between the Raman scattered and the initial O VI line component. For this we have to determine first the observed flux ratios $F_{\lambda6825}/F_{\lambda1032}$ and $F_{\lambda7082}/F_{\lambda1038}$ and apply an interstellar reddening correction which is derived in the following section. Line fluxes, reddening corrections and resulting efficiencies are summarized in Table 7. Uncertainties are only listed for the resulting efficiencies, but they account for the uncertainties in the line fluxes and E(B–V) as given in the corresponding Tables 2, 3 and 6 and in the text of Sect. 7.

8.1. Correction for interstellar reddening

The accuracy of the determined Raman scattering efficiency depends sensitively on a precise interstellar reddening correction. We have therefore compiled in Table 6 reddening determinations from the literature. The chosen values are mainly based on the interstellar 2200 Å absorption feature in IUE spectra. The indicated uncertainty in the E(B–V)-values reflect the scatter between the determinations of different authors, who might even have used the same spectra.

We use for the extinction correction the "average" extinction curve of Seaton (1979). We should, however, expect position dependent deviations from this curve (e.g. Massa 1987), but this effect seems to be negligible in comparison to other uncertainties.

For the reddening of CD$-43°14304$ only an upper limit has been determined previously. Therefore, we determine here the reddening of this objects from the He II line $\lambda1085$ from ORFEUS (Table 3) and the quasi-simultaneous ESO-observations of the He II λ6683 line (Table 5). The line flux ratio according to

Table 6. Compilation of the interstellar reddening values. The adopted values are given in bold figures.

Object	E(B-V)	Reference
Z And	**0.30**±0.05	
	0.30±0.05	Altamore et al. (1981)
	0.29±0.10	Kenyon & Webbink (1984)
	0.30	Mürset et al. (1991)
AG Dra	**0.04**±0.02	
	0.03±0.01	Kenyon & Webbink (1984)
	0.06±0.02	Viotti et al. (1984)
	0.00	Mürset el al. (1991)
	0.03	Leibowitz & Formiggini (1992)
	0.03	Kafatos et al. (1993)
	0.05	Mikolajewska et al. (1995)
RR Tel	**0.10**±0.02	
	0.10±0.02	Penston et al. (1983)
	0.10	Mürset el al. (1991)
AG Peg	**0.11**±0.04	
	0.12±0.03	Keyes & Plavec (1980)
	0.12	Slovak & Lambert (1982)
	0.15±0.04	Kenyon & Webbink (1984)
	0.08±0.04	Penston & Allen (1985)
	0.05	Mürset el al. (1991)
	0.10±0.05	Kenyon et al. (1993)
V1016 Cyg	**0.30**±0.10	
	0.28	Nussbaumer & Schild (1981)
	0.17±0.02	Kenyon & Webbink (1984)
	0.40	Mürset el al. (1991)
CD−43° 14304	**0.14**±0.06	
	<0.2	Schmid & Nussbaumer (1993)
	0.14±0.06	He II lines (this work)

the case B recombination theory is $F(\lambda1085)/F(6683) = 158$ for the nebular parameters $T_e = 20000$ K and $N_e = 10^9\,\mathrm{cm}^{-3}$ (Hummer & Storey 1987). From the measured He II ratio the reddening parameter $E(\mathrm{B-V}) = 0.14$ is obtained. The same procedure gives for RR Tel a reddening of $E(\mathrm{B-V}) = 0.08$ in good agreement with other determinations. An extinction determination for Z And based on the He II lines was also made by Birriel et al. (1998), who obtained $E(\mathrm{B-V}) = 0.24 \pm 0.03$. This value is again close to results quoted in Table 6 based on the 2200 Å feature compensation technique. Thus we adopted for CD−43°14304 $E(\mathrm{B-V}) = 0.14 \pm 0.06$ from the He II lines, where the error accounts for the line flux uncertainties.

We note that the He II λ4686 line flux in CD−43°14304 is significantly higher than expected from case B recombination theory. This could be caused by a resonance fluorescence effect, where H I Lyα photons pump the He II 2–4 transition followed by a He II 4–3 λ4686 decay. This process requires a highly populated metastable $2s\,^2$S level of He II, which is not unlikely at the high nebular densities in CD−43°14304. The employed He II λ1084 and λ6683 lines should be at most little affected by resonance fluorescence or other radiative transfer (self-absorption) effects. Nonetheless we adopt quite a large uncertainty for the derived reddening parameter of CD−43°14304.

8.2. Efficiencies

The derived Raman scattering efficiencies N_{6825}/N_{1032} and N_{7082}/N_{1038} are given in the last two columns of Table 7. For this the dereddened line flux ratios were converted into photon flux ratios. Because the O VI λ1038 transitions in V1016 Cyg and Z And are strongly affected by interstellar absorptions we adopted for the intrinsic λ1038 photon flux $N_{1038} = N_{1032}/2$ as expected for the (optically thin) O VI doublet line ratio.

For RR Tel and AG Dra line fluxes and the interstellar extinction are well known so that the derived efficiencies are relatively accurate. For the other objects the precision is significantly lower mainly due to the uncertainties in the reddening correction. Different observations for a given object show no temporal variations in the line ratios $F_{\mathrm{Raman}}/F_{\mathrm{OVI}}$ beyond the measuring errors.

RR Tel, Z And and V1016 Cyg have a $\lambda1032 \rightarrow \lambda6825$ conversion efficiency of about $5\% - 10\%$ and about a third of this value for the $\lambda1038 \rightarrow \lambda7082$ process. The values for RR Tel and Z And are in agreement with the results of Espey et al. (1995) and Birriel et al. (1998) from HUT-measurements. The higher Raman scattering efficiency for the $\lambda1032 \rightarrow \lambda6825$ process can be explained by the larger scattering cross section when compared to the $\lambda1038 \rightarrow \lambda7082$ process.

For AG Dra the Raman scattering efficiencies N_{6825}/N_{1032} and N_{7082}/N_{1038} are both close to 50%, significantly higher than in the objects discussed above. In this system, one out of three escaping O VI photons is Raman scattered. Also CD−43°14304 has a high $\lambda1032 \rightarrow \lambda6825$ scattering efficiency of about 25%. Another common specialty of AG Dra and CD−43°14304 is that the N_{6825}/N_{1032} and N_{7082}/N_{1038} scattering efficiencies are practically equal. This follows from the low Raman line ratio of $F(6825)/F(7082) = 2.4$–2.9 (Table 7), which is not much larger than the expected O VI line ratio. Typically the Raman line ratio is more like 4–5 in symbiotic systems (Allen 1980). In the Raman line surveys of Schmid & Schild (1994) and Harries & Howarth (1996b) only AG Dra, CD−43°14304 and possibly SY Mus (large error) have a $F(6825)/F(7082)$-ratio below three. This could indicate that high Raman scattering efficiencies are coupled with low $F(6825)/F(7082)$-ratios. AG Dra has a tag as outstanding symbiotic system, because it is a halo binary with low metallicity and contains a red giant with a relatively early spectral type (e.g. Smith et al. 1996). CD−43°14304 has also a red giant with an early spectral type, a high galactic latitude and other properties similar to AG Dra (Schmid & Nussbaumer 1993).

The derived scattering efficiencies can be compared to the grid of model calculations published in Schmid (1996). The efficiencies for RR Tel, Z And and V1016 Cyg suggest that about one out of three emitted O VI λ1032 photons interact with the scattering region. This implies that the neutral scattering region as seen from the O VI emission region covers about a third of the sky, comparable to a circular sky region with a diameter of roughly 140°. This corresponds approximately to a scattering geometry between the models XB3 and XC3 of Schmid (1996).

Table 7. Measured fluxes for the O VI lines and estimated fluxes for the Raman scattered O VI lines in units of $10^{-12}\,\mathrm{erg\,cm^{-2}\,s^{-1}}$. E(B–V) is the adopted interstellar extinction and $N_{\mathrm{Raman}}/N_{\mathrm{O\,VI}}$ the derived Raman scattering efficiency expressed as a percentage. Orbital phase $\phi = 0$ corresponds to light minimum when the cool component is in front of the hot component.

Object	date	orbital	OVI		Raman		E(B–V)	$N_{\mathrm{Raman}}/N_{\mathrm{O\,VI}}$	
		phase	1032	1038	6825	7082	[mag]	N_{6825}/N_{1032}	N_{7082}/N_{1038}
RR Tel	93-09-16		256	154	7.2	1.2	0.10	$6.9 \pm 2.2\%$	$2.1 \pm 0.8\%$
RR Tel	96-11-21		218	132	4.5	0.9	0.10	$5.0 \pm 1.6\%$	$1.7 \pm 0.6\%$
AG Dra	93-09-18	0.18	95	42	10.5	4.4	0.04	$49 \pm 17\%$	$48 \pm 17\%$
AG Dra	96-11-21	0.28	62	21	7.0	2.9	0.04	$49 \pm 30\%$	$32 \pm 20\%$
AG Peg	93-09-16	0.51	95	42	< 2	< 2	0.11	$< 7\%$	$< 18\%$
AG Peg	96-11-23	0.93	43.4	24.7	1.4	< 1	0.11	$7 \pm 4\%$	$< 16\%$
Z And	93-09-17	0.67	25	2.5	4.5	1.2	0.30	$6 \pm 3\%$	$3 \pm 2\%^{+}$
Z And	96-12-01	0.21	35.5	4.2	4.5	1.2	0.30	$4 \pm 2\%$	$2 \pm 1\%^{+}$
V1016 Cyg	96-11-30		19	1.0	3.5	0.5	0.30	$7 \pm 5\%$	$2 \pm 1\%^{+}$
CD$-43°14304$	96-11-23	0.35	10.3	7.3	1.7	0.6	0.14	$27 \pm 18\%$	$11 \pm 7\%$

$+$: assuming an initial photon flux ratio $N_{1038} = N_{1032}/2$; Orbital phases according to the ephemerides of Meinunger (1979) for AG Dra, Fernie (1985) for AG Peg, Formiggini & Leibowitz (1994) for Z And, and Schmid et al. (1998) for CD$-43°14304$. The orbital elements for the D-type systems RR Tel and V1016 Cyg are not known or highly uncertain (see Schild & Schmid 1996; Schmid 1998).

The high efficiencies derived for AG Dra and CD$-43°14304$ are only expected if the O VI region is surrounded by dense neutral gas where Raman scattering can take place. However, such a dense H^0-shell would also produce a strong Rayleigh scattering absorption near Lyα of the continuum radiation from the hot component. AG Dra was frequently observed with IUE, but this effect has never been detected. An alternative possibility is that only the O VI region was heavily obscured, during the ORFEUS-runs, but not the hot component, e.g. by parts of the neutral wind from the cool giant.

According to the model calculations the Raman scattering efficiency depends on the orbital phase. Unfortunately we have not enough data to investigate this problem. In addition the systems AG Dra, Z And and AG Peg are known to be non-eclipsing and the possible changes in the Raman scattering efficiency may be rather subtle.

8.3. AG Peg

The Raman scattering efficiency $N_{6825}/N_{1032} \approx 7\%$ derived for AG Peg is comparable to the values for Z And, RR Tel and V1016 Cyg. In AG Peg the O VI emission consists of a narrow nebular component and a broad wind component. But the λ6825 Raman line in AG Peg displays only a narrow nebular component. No signature of a broad wind line is visible. This indicates that the Raman scattering efficiency is higher for the nebular component than for the wind component. Fig. 11 illustrates this with a comparison of the line profiles of the direct O VI λ1032 emission and the Raman scattered emission at λ6825.

According to Sect. 4.3 (Fig. 3) only about 30% of the total O VI λ1032 line flux is nebular in origin. Consequently, the Raman scattering efficiency for the nebular emission is about

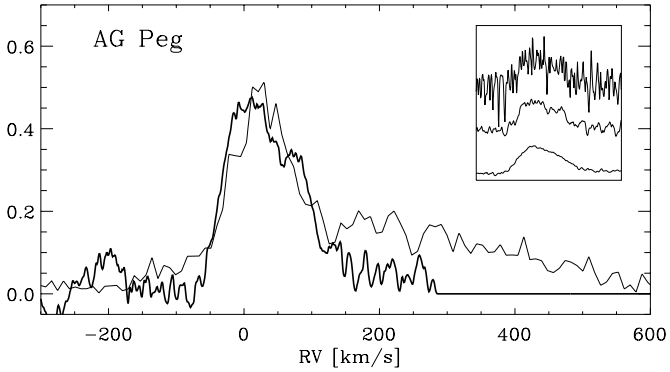

Fig. 11. Raman scattered O VI λ6825 line (thick curve) and the original O VI λ1032 line (thin) in AG Peg. For λ6825 a boxcar smoothing with a total width of $30\,\mathrm{km\,s^{-1}}$ (corresponding to 4.5 Å or 15 pixels in the original spectrum) has been applied. The flux of the λ6825 line is scaled such that it is comparable to the narrow nebular component in the O VI λ1032 line. For $\mathrm{RV} > 200\,\mathrm{km\,s^{-1}}$ the extracted Raman line spectrum is strongly affected by the atmospheric B-band. Inset: Original Raman line and profiles smoothed with 15 and 60 $\mathrm{km\,s^{-1}}$ wide boxcar functions.

$N_{6825}/N_{1032} \approx 23\%$. This is comparable to the values derived for AG Dra and CD$-43°14304$ and much higher than for Z And, RR Tel and V1016 Cyg. It should however be kept in mind that the error N_{6825}/N_{1032} is rather large for AG Peg due to the uncertainties in the interstellar extinction and the Raman line flux.

A more accurate statement can be made about the relative Raman scattering efficiency between nebular and wind component. The comparison of the line profiles in Fig. 11 suggests that the Raman scattered emission of the broad wind component would be visible if its strength relative to the narrow emission

is half or more compared to the relative strength in the original O VI emission. This finding is equivalent with the statement that the Raman scattering efficiency is at least two times higher for the nebular component than for the wind component.

The high Raman scattering efficiency for the narrow emission component indicates that the nebular region is closer to the Raman scattering region than the wind emission of the hot component. A tentative model geometry based on this conclusion is shown in Fig. 16c.

9. Line structure of the Raman scattered lines

The analysis of the Raman line structures is based on the ESO-CASPEC spectra of RR Tel and CD$-43°14304$ plotted in Figs. 9 and 12. For Z And the mean profile of Schmid & Schild (1997b) is adopted. Similarly a mean profile is constructed for AG Dra from the four pre-outburst observations (401,501,601,701) described in Schmid & Schild (1997a). Temporal variations of the Raman line structure are seen for example in AG Dra. But during quiescence these changes are relatively small. For AG Peg we use the intensity profile extracted from the WHT-data as described in Sect. 7.6 and smoothed as shown in Fig. 11. For this object it is not possible to provide a detailed line structure, but only line widths and line centers.

In previous studies it was found that the Raman lines in symbiotic systems show often a multi-peaked structure (see e.g. Allen 1980; Harries & Howarth 1996b). Usually the profiles consist of a main (central) peak with an adjacent weaker component on the blue side and sometimes also one on the red side. In some systems the blue component forms a distinct maximum like in RR Tel (e.g. Fig. 12), but often it is only a "shoulder" as in AG Dra, CD$-43°14304$ and Z And (Fig. 13). The strength of the red component varies strongly from object to object, some having profiles with a clear secondary maximum in the red, some having a red "shoulder" as in Z And, and many objects showing no clear signature of a red component at all.

In a given object the two Raman lines λ6825 and λ7082 display a qualitatively similar structure. Two examples are shown in Fig. 11, which compares for RR Tel and CD$-43°14304$ the normalized λ6825 and λ7082 Raman line radial velocity structures. These spectra were obtained by subtracting an unstructured stellar continuum from the ESO Caspec spectra shown in Fig. 9. This procedure leaves many narrow photospheric absorptions, particularly in the blue portion of the λ7082 component where molecular TiO bands show a strong, quasi-periodic wave structure. It seems that in RR Tel the relative strength of the blue portion of the λ7082 line is somewhat weaker than in the λ6825 line. This may be explained as attenuation by TiO transitions in the atmosphere and wind of the cool giant.

We conclude, that the Raman line structure of the λ7082 component does not differ qualitatively from the structure of the λ6825 component. There exist quantitative differences which are, however, in most cases rather subtle. Therefore, we neglect in the following the λ7082 component, because it is burdened with larger uncertainties due to the TiO absorptions. Further it should be noted that also the structure of the corresponding

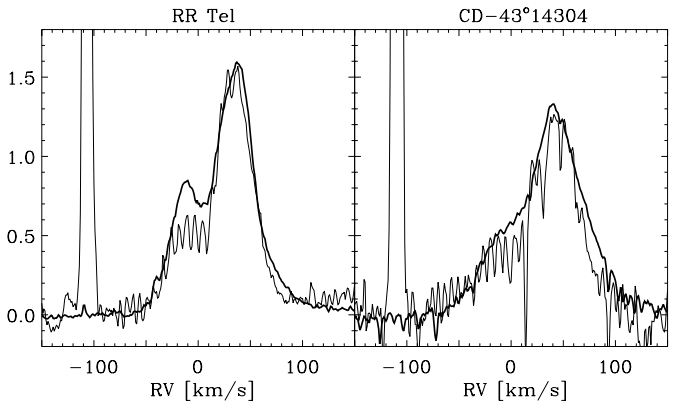

Fig. 12. Normalized profiles of the Raman scattered O VI lines λ6825 (thick line) and λ7082 (thin) in RR Tel and CD$-43°14304$. The radial velocity scale corresponds to the systemic velocity space of the original O VI lines. The relative flux of the λ7082 has been multiplied by 4.5 for RR Tel and 2.9 for CD$-43°14304$.

Table 8. Line center and line width for the Raman scattered O VI line λ6825. For the RV values also the parameters for the corresponding O VI λ1032 line from Table 4 is given.

line param.	AG Dra	RR Tel	CD$-43°$ 14304	AG Peg	Z And
			line center		
heliocentric in Å					
λ6825	6827.7	6828.2	6831.9	6829.2	6830.4
systemic in RV$_c$ [km s^{-1}]					
λ6825	+38	+28	+38	+27	+33
λ1032	+49	+27	+40	+29	+57
			line width (FWHM)		
$\Delta\lambda$ in Å					
λ6825	12.3	10.7	12.0	$\sim 18^{+}$	15.1
RV in km s^{-1}					
λ6825	82	72	80	$\sim 120^{+}$	101
λ1032	71	55	93	~ 95	78

+: the measured width for AG Peg depends strongly on the procedure for subtraction of a red giant spectrum and smoothing of the residual signal (the estimated uncertainty is about 20%)

O VI line at λ1038 is often affected, in this case by interstellar absorptions. This causes additional uncertainties when studying differences between the far-UV and Raman-scattered O VI line profiles. Nonetheless, a future study should address the quantitative differences between the $\lambda 1032 \rightarrow \lambda 6825$ and the $\lambda 1038 \rightarrow \lambda 7082$ Raman scattering processes.

Table 8 summarizes the measured centers and widths for the Raman λ6825 lines. The FWHM were determined by fitting a Gaussian profile to the λ6825 line. The results were compared with other measuring procedures. For example the line center was defined by the wavelength which divides the Raman line in two parts with equal flux, or the line width was determined as minimum wavelength interval which includes 76% of the line flux (as for the FWHM-interval of a Gaussian line). The found values differ by less than 0.3 Å for the line centers and less

than 5% for the line widths from the values given in Table 8. Nonetheless, it should be noted that there exists some ambiguity in defining "the" center or width for a feature with complex morphology.

The mean central wavelength for the λ6825 feature in our five objects is 6829.5 Å. The same value was already found by Allen (1980) and similar redshifts are also reported in the survey of Harries & Howarth (1996b).

9.1. Velocity conversion

The λ6825 line parameters in Table 8 are also given in the systemic radial velocity space of the original O VI λ1032 line. For this conversion we use the relation

$$\mathrm{RV_{OVI}} = (\mathrm{RV_{Raman}} - \mathrm{RV_{sys}})/6.614\,.$$

$\mathrm{RV_{Raman}}$ is the RV displacement or width measured with respect to the rest wavelength 6825.44 Å of the Raman transition, and $\mathrm{RV_{sys}}$ the adopted systemic velocity of the studied objects as given in Table 4. The division by the quotient $\lambda_{\mathrm{Raman}}/\lambda_{\mathrm{OVI}} = 6.614$ re-establishes the O VI RV scale, which was stretched by this value in the Raman scattering process. For the weaker Raman line the corresponding quotient is 6.828 and the exact rest wavelength is 7082.40 Å (Schmid 1989). Thus, 0.15 Å in the λ6825 Raman line and 0.16 Å in the λ7082 Raman line are equivalent to 1 km s^{-1} on the RV-scale of the corresponding O VI line.

10. Comparison of direct and Raman scattered O VI line profiles

The systemic line centers RV_c of the direct and the Raman scattered O VI lines are shifted to the red by a value lying between about 25 and 60 km s^{-1}. The redshifts of the λ6825 feature and the O VI λ1032 line agree very well for RR Tel, CD$-43°14304$ and the narrow nebular component in AG Peg. The difference between RV_c for λ6825 and λ1032 in AG Dra is not significant in view of the uncertainty in the absolute wavelength calibration for the O VI observations. The corresponding difference $\mathrm{RV}_c(\mathrm{O\,vi}) - \mathrm{RV}_c(\lambda6825) = 24\,\mathrm{km\,s^{-1}}$ in Z And seems to be real.

Measured line widths range between 70 km s^{-1} and 120 km s^{-1} for the Raman lines, and between 55 km s^{-1} and 100 km s^{-1} for the O VI line. The latter values have been corrected for the expected instrument broadening. The measuring uncertainties for these line widths are less than 5 km s^{-1}, except for AG Peg. In this object the line widths are less accurate ($\pm$20 km s^{-1}), because of the additional wind component in the $\lambda1032$ line and the weakness of the λ6825 feature.

In 4 out of 5 systems the λ6825 line is broader than the corresponding O VI emission. The additional width for the Raman line is 15% in AG Dra, 30% for RR Tel and Z And, and about 25% for the nebular component in AG Peg. A comparison of the line profiles plotted in Figs. 13 and 14 indicates that the extra width of the Raman lines in these objects could be explained by a blue line component in the λ6825 feature, which is not present in the O VI line. In CD$-43°14304$ a weak blue component seems to be present not only in the Raman line but also in the O VI line. Correspondingly the Raman line in this object is similar to the O VI emission.

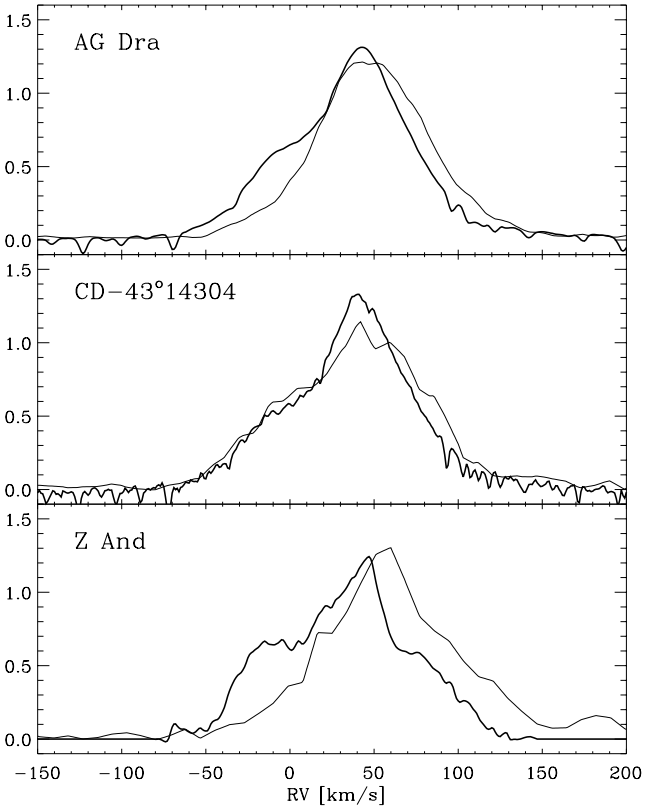

Fig. 13. Raman scattered O VI λ6825 line profile (thick curve) and the original O VI λ1032 line (thin) in AG Dra, CD$-43°14304$ and Z And. The radial velocity scale corresponds to the systemic velocity space of the original O VI line. The flux of all lines is normalized to the same total line flux.

RR Tel displays strong qualitative differences between the O VI λ1032 line and the corresponding Raman line. The initially single–peaked O VI line is transformed into a double–peaked λ6825 emission. The RV of the peaks in the λ6825 profile are at -11 km s^{-1} and $+38$ km s^{-1}. The central minimum at $+5$ km s^{-1} is practically at the rest velocity.

10.1. Origin of profile differences

Different processes may be put forward for explaining the line profile differences between the O VI lines and their Raman scattered counterparts. Here we consider three possibilities in more detail: (i) absorption by line transitions, (ii) Doppler shifts introduced in the Raman scattering process, and (iii) non-isotropic O VI line emission.

Line absorptions may alter the structure of the resulting Raman line profiles. For example, neutral, singly ionized atoms or molecules in the scattering region could absorb either the incoming O VI or the Raman scattered photons. If Raman scattered photons are absorbed, we expect to see narrow absorptions in

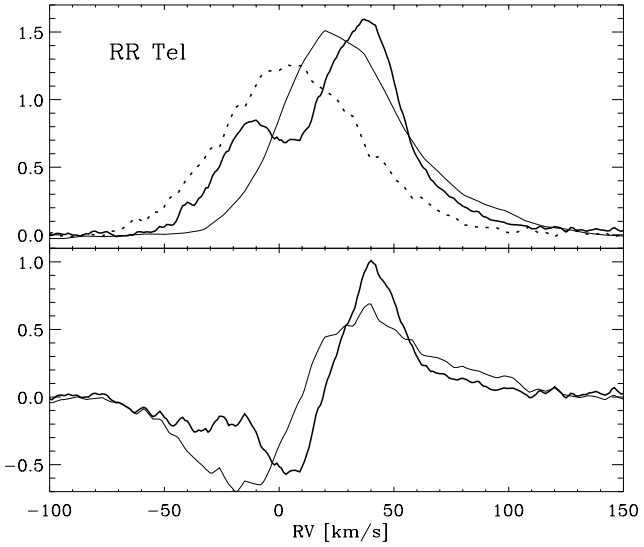

Fig. 14. Top: Raman scattered O VI λ6825 line (thick curve), the original O VI λ1032 line (thin) and the O V λ1643 recombination line in RR Tel. The flux of all lines is normalized to the same total line flux. Bottom: Difference spectra $F_n(\lambda 6825) - F_n(\mathrm{O\,V})$ and $F_n(\mathrm{O\,VI}) - F_n(\mathrm{O\,V})$. The radial velocity scale corresponds to the systemic velocity space of RR Tel ($\lambda 6825$ corrected for the Raman scattering shift).

the Raman profile. Such additional absorptions due to TiO may be present in the blue wing of the λ7082 component (Fig. 12). However, the stronger component is practically free of such absorptions, as suggested by the smooth λ6825 profile in RR Tel, and in other systems where the Raman line is so strong that the photospheric spectrum from the cool giant is negligible. If O VI photons are strongly absorbed by line transitions, then this would cause broad minima in the resulting Raman lines. But this would only affect one Raman line at a given radial velocity. Therefore, this cannot be an important effect for changing the overall profiles of the Raman lines since the radial velocity structure of both components are qualitatively the same.

A Doppler shift will be introduced in the Raman scattering process by the motion of the scattering H^0-atoms relative to the direction of the incoming O VI photon. Doppler shifts due to the large scale motion in the cool giant's wind were already put forward to explain the polarization structure in the Raman lines (Schmid & Schild 1994). According to Monte Carlo simulations, the observed polarization structure can be modeled for a cool giant's wind velocity of about 20 km s^{-1}. In this model the neutral scattering region between the two stars moves towards the O VI region while the outer wind region moves away from it. The models predict a broadened and slightly redshifted (by $\Delta \mathrm{RV}_{\mathrm{OVI}} \approx 10$ km s^{-1}) Raman line relative to the initial O VI line (see Schmid 1996). Such Doppler shifts could explain in AG Dra, AG Peg and Z And the slightly broadened λ6825 Raman lines. Doppler shifts could also explain the systematic RV shift between the λ6825 and λ1032 lines in Z And, if Raman scatterings occur mainly in a region which moves with 25 km s^{-1} towards the O VI region. However it is shown below that also radiative transfer effects can at least partly explain these effects.

Doppler shifts alone cannot explain the differences in the O VI λ1032 and the λ6825 Raman line structure seen for RR Tel. It is impossible to transform one broad line component with Doppler shifts into two narrow components. A very attractive explanation is however, that the neutral scattering region in RR Tel could "see" a different λ1032 and λ1038 line profile from the O VI emission region than an observer far outside the binary system. This implies, of course, that the O VI nebulosity is not spherically symmetric.

Radiative transfer effects in the O VI resonance lines can easily produce direction dependent line profiles, as soon as some anisotropy is present. As shown in Sect. 4.2 line absorption and scattering in an expanding medium is most likely responsible for redshifted O VI lines. This is also illustrated in the lower panel of Fig. 14, which shows the differences between an optically thin O V recombination line and the O VI λ1032 resonance line. The resulting curve has some similarities with a P-Cygni line with an expansion velocity of $v \approx 70$ km s^{-1}. The difference between the Raman scattered line and O V resembles more a P-Cygni line with a smaller expansion velocity of about $v \approx 30$ km s^{-1}. The conclusion is that we see via the Raman scattering process a projected profile, which differs from the directly observed profile. In the direct O VI line the absorption component attenuates fully the line profile from roughly -10 km s^{-1} to at least -70 km s^{-1} as expected for a slowly expanding nebulosity. Contrary to this the H^0-atoms located in the vicinity of the red giant reflect an O VI line with an absorption component at $+5$ km s^{-1}, which is close to the rest velocity.

Further support for a substantial anisotropy in the emission nebula of RR Tel comes from observations of other Raman scattered lines by van Groningen (1993). He detected a single–peaked, broad line around 4850 Å due to Raman scattered He II λ972 and a broad, double–peaked line around 4975 Å due to Raman scattered C III λ977. Thereby the observed line widths and strengths are consistent with the Raman scattering interpretation. In the ORFEUS Echelle spectrum of RR Tel the C III λ977 line is single–peaked like the He II λ1085, λ992 or λ959 recombination lines. This indicates that radiative transfer changes strongly the structure of the C III line as expected for a resonance transition, but not or much less the optically thin He II recombination line.

Thus, anisotropic O VI emission plays a key role for understanding the line profile differences between the O VI lines and their Raman scattered counterparts in RR Tel. Therefore we should also expect that this anisotropy effect can contribute, besides the H^0-Raman scattering Doppler shifts, to profile differences seen in other objects.

10.2. Further hints from the line polarization structure

The observed Raman line polarization structures of AG Dra, Z And, RR Tel and other systems have been analyzed and modeled in detail in various papers (e.g. Schmid & Schild 1994,1997a,b; Schmid 1996; Harries & Howarth 1996a,b, 1997; Lee & Lee

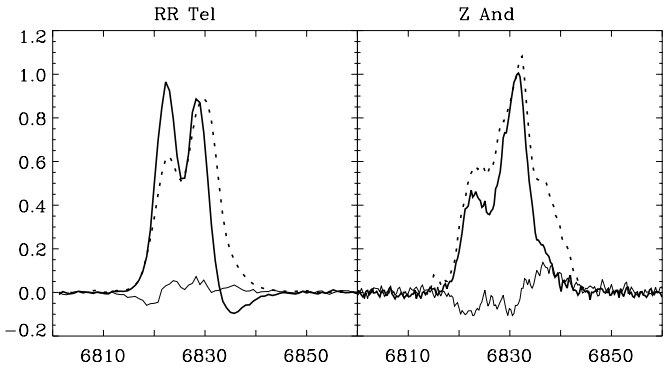

Fig. 15. O VI λ6825 Raman line polarization structures in RR Tel and Z And given as normalized and 'rotated' Stokes Q (thick line) and Stokes U (thin line) spectra in a coordinate system aligned with the systemic position angle of polarization. The dotted lines are the corresponding normalized intensity spectra, divided by a factor of 10.

1997). Therefore we point here only to an important fact, which further supports the above argument, that strong anisotropic line emission from the O VI region is present.

Fig. 15 shows the λ6825 Raman line of RR Tel and Z And in the 'rotated' Stokes parameters Q' and U' in a coordinate system aligned with the systemic position angle of polarization (see Schmid 1996; Schmid & Schild 1997b).

In polarized light the Raman line of RR Tel displays even more clearly a structure which resembles an emission line with a central absorption. Moreover, this type of polarization structure is even present in the Raman lines of Z And. What is only a blue shoulder in the intensity profile is in polarized light a distinct blue component separated by a clear minimum from the main component. Similarly the λ6825 Raman line in CD$-43^\circ 14304$ shows in polarized light a narrow central minimum, which is not visible in the intensity profile (Harries & Howarth 1996b).

For our interpretation of the λ6825 line polarization structure we recall the basic model for Raman scattering in symbiotic systems. In this model the O VI radiation penetrates from the hot component side into the neutral scattering region near the cool giant, where transformation into the Raman lines occur. Therefore, the main scattering region is expected to be the irradiated outer atmosphere of the cool giant facing the hot component. The produced polarization direction is perpendicular to the direction of the incoming light or in this case, perpendicular to the binary axis (the line connecting the two stars). Scatterings in other regions, e.g. further away from the cool giant and the binary axis will contribute as well to the resulting Raman line. But these scattering regions produce at least partly other polarization directions, e.g. tilted by about 45°. Such polarization contributions can be geometrically compensated in a scattering geometry with some symmetry with respect to the binary axis (for more details see Schmid & Schild 1994; Schmid 1996). From this it can be concluded that the polarized line profile may provide a selection of predominantly those Raman photons, which are produced in the central, main scattering region near the cool giant.

Thus, the double–peaked structure of the polarized line profiles in RR Tel and Z And and CD$-43^\circ 14304$ can be interpreted as well defined projection of the O VI line region as seen from the cool giant. The corresponding intensity profile is more smeared because it reflects an average of the different profiles seen by the entire Raman scattering region.

The situation may be somewhat more difficult for AG Dra. The Raman scattering efficiency for this object indicates that a very large fraction of O VI photons are Raman scattered. This may only be possible if the scattering region is very extended so that also O VI photons moving perpendicular to the binary axis are scattered. But this would produce a polarization component with a direction parallel to the binary axis, and thus compensate for the polarization signal from the irradiated region near the cool giant. This possibility is supported by the fact that the Raman line polarization is reduced to a level of about $p \approx 3\%$ in AG Dra, much lower than the typical values 6–10% measured in RR Tel, Z And or CD$-43^\circ 14304$ (see Harries & Howarth 1996b; Schmid & Schild 1997a,b). Thus, it is possible that the polarization profile in AG Dra is complicated by this compensation effect and therefore not representative of the O VI line profile, as seen from the scattering region.

10.3. The scattering geometry

In the previous sections we found that the presence of anisotropic O VI line emission is of prime importance for understanding the Raman line structure. According to this the O VI line has a different structure when viewed directly as far-UV emission compared to the Raman line emission produced via scattering in the neutral atmosphere and wind of the cool giant. Fig. 16 provides strongly simplified, schematic models for symbiotic systems in order to illustrate the following discussion on the scattering geometry. The considered models assume, as suggested by photoionization calculations (Seaquist et al. 1984; Nussbaumer & Vogel 1987,1990), that the O VI emission region is located around the hot component or between the hot component and the cool giant. The assumed gas flow pattern in the O VI region are for Fig. 16a and b just the simplest ones for binaries, being basically a radial outflow from one of the two components. The model in Fig. 16c is inspired by the interacting wind models put forward by Girard & Willson (1987), Nussbaumer & Walder (1993), or Mürset et al. (1995).

In the direct O VI line we see an overall expansion of the emission region with a velocity of about 30–60 km s^{-1} or a bit more. This is suggested by the observed systematic redshift of the O VI emission due to a radiative line transfer effect. Many symbiotic systems show the same effect in the C IV and N V resonance lines (see Friedjung et al. 1983). It seems therefore that radial motions are a rather common property of these nebulae.

The simplest geometry for producing redshifted O VI resonance lines and undisplaced optically thin nebular lines is an expanding and spherically symmetric nebula centered around the hot component as shown in Fig. 16a. The emitted O VI line profile from such a geometry is direction independent. In this model the differences between direct and Raman scattered line

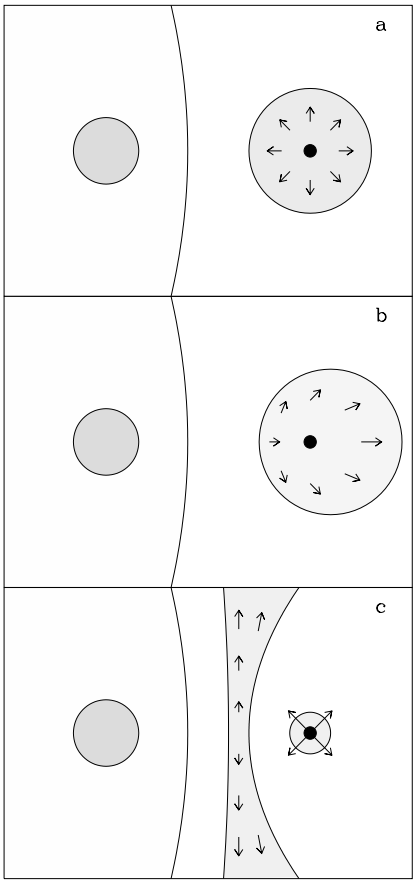

Fig. 16a–c. Schematic scattering geometries for symbiotic systems. In all panels the cool giant and the neutral scattering region are given to the left as dark shaded circle and light shaded area respectively. The hot component is the dark dot to the right. The geometric shape and flow pattern of the O VI emission region is illustrated as shaded region with arrows.

profiles must be explained by Doppler shifts due to systematic motion of the H^0-atoms in the neutral scattering region.

However, this model is not able to produce direction dependent O VI emission line profiles. The model sketched in Fig. 16b can produce direction dependent line profiles. There it is assumed that the gas streams radially from the cool giant towards the hot component where it may be further accelerated away from the hot component, for example by radiation pressure or a stellar wind. An outside observer would still see for most line of sights a redshifted O VI line. But towards the cool component the O VI emission and the resulting Raman scattered emission could show redshifted profile with a central self-absorption near the systemic velocity as observed in RR Tel.

For AG Dra, Z And and CD$-43^\circ 14304$ the differences in the line profiles of the direct and the Raman scattered O VI emissions are less pronounced compared to RR Tel. For these objects we may therefore assume an O VI gas flow pattern intermediate between those of Fig. 16a and b. It is interesting to note that AG Dra, Z And and CD$-43^\circ 14304$ contain cool giants for which only moderate mass loss rates are expected. RR Tel on the other hand contains a Mira variable as cool giant, which undergoes most likely very strong mass loss. This may be a hint that model geometries like in Fig. 16b and strong differences in the direct and Raman scattered emission may be related to the mass loss rate of the cool giant.

In AG Peg the O VI line emission consists of a nebular and broad wind component, while the Raman scattered emission displays only a nebular component. From this we conclude that the broad O VI wind emission is further away from the neutral scattering region, so that the Raman scattering efficiency is reduced (see Sect. 8.3). There is no doubt that the broad wind emission originates from the hot components' wind. Consequently the nebular O VI emission region must be located about half way between the two stellar components. This finding strongly supports the colliding wind model of Mürset et al. (1995) for AG Peg, which was adopted for the schematic model drawn in Fig. 16c.

11. Summary and conclusions

The outstanding properties of the O VI Raman scattering process provide many new opportunities for determining the geometric structure of symbiotic systems, which are mentioned in the Introduction (Sect. 1) and reviewed in more detail in Schmid (1998). In this paper we concentrate on the new diagnostic possibilities offered by far-UV observations of the O VI $\lambda\lambda$1032,1038 emission lines.

From our ORFEUS data we have determined the O VI line fluxes for a small, but quite representative, sample of symbiotic systems. From the measured and dereddened line fluxes of the direct and Raman scattered O VI lines we derived the Raman scattering efficiency. This parameter is a sensitive measure of the size of the neutral scattering region in symbiotic systems. The efficiencies for RR Tel, V1016 Cyg and Z And are about 5–10% for the $\lambda 1032 \rightarrow \lambda 6825$ conversion and about 1–4% for $\lambda 1038 \rightarrow \lambda 7082$. This suggests that about 30% of the released O VI λ1032 photons interact in the neutral scattering region around the cool giant. The Raman scattering efficiency is much higher, up to 50%, for AG Dra and CD$-43^\circ 14304$. These high values may indicate that the O VI region is embedded in the neutral scattering region. This suggests that the main part of the O VI emission region is located between the cool giant and the ionizing source, and is not surrounding completely the ionizing component as shown in Fig. 16a and b. This modification does not contradict the previous discussion on line structures provided that the flow pattern in the O VI nebula relative to the neutral scattering region is not changed. Based on numerical calculations it is expected that the emission line region is close to the cool component if either the mass loss rate of the cool giant is low or/and the ionizing flux very high (see e.g. Nussbaumer & Vogel 1990).

With the ORFEUS-II Echelle data we were able to investigate for the first time the O VI emission line structure of symbiotic systems in the far-UV. Therefore, these data close an important observational gap for the investigation of the Raman scattering process in symbiotic systems.

The direct observation of the O VI emission region revealed a systematic redshift in the O VI lines. This can be explained as radiative line transfer effect in a slowly expanding medium.

The Raman scattered lines provide in addition an indirect view of the O VI emission region via the central scattering region. The comparison of the line profiles in RR Tel suggest strongly that two different gas flow patterns of the O VI region are seen in the direct and the Raman scattered emission. The double–peaked structure of the Raman line can be interpreted as O VI emission with a central self-absorption, indicating that the gas in the O VI region is not expanding towards the cool component. The presence of such direction dependent O VI absorption features could be a general property of symbiotic systems because the Raman lines show often profiles with multiple peaks.

The possibility of direction dependent O VI emission has not been considered in previous studies on the Raman scattering geometry of symbiotic systems. For example, the basic polarization structure in the Raman lines was only attributed to the Doppler shifts introduced by the systematic motion of the scattering H^0-atoms (e.g. Schmid & Schild 1994; Schmid 1996; Harries & Howarth 1996b, 1997; Lee & Lee 1997a,b). The corresponding scattering model assumed a spherically expanding neutral wind from the red giant which is ionized and illuminated by O VI photons from the hot components side. The Raman photons in the blue line wing originate in the neutral region between the two stars. This region is illuminated along the binary axis and the O VI photons are Doppler shifted by approaching H^0-atoms. The resulting Raman photons are therefore blue shifted and have a polarization perpendicular to the binary axis. Scatterings by receding H^0-atoms in the outer wind regions produce the photons in the red line wing. The polarization direction in the red wing depends on the extent of the neutral scattering region. A polarization parallel to the binary axis is expected for systems with very extended neutral regions, where also O VI photons propagating away from the binary axis can be Raman scattered. A detailed discussion on the merits of this scattering model is given in Schmid (1996).

The same line polarization structure may also be obtained with scattering models considering only direction dependent O VI emission and neglecting Doppler shifts due to the scattering H^0-atoms. Such a model assumes that the central scattering region "sees" O VI profiles which are not or only slightly redshifted. A larger redshift is "seen" by the outer scattering region as observed for the direct O VI emission.

Thus the two scattering models described above are identical except for the origin of the systematic wavelength difference between the Raman photons with different polarization directions attributable to the central and outer H^0 scattering regions. Probably both effects, direction dependent O VI emission and Doppler shifts due to the systematic motion of the H^0-atoms are present simultaneously in a given object. This should be taken into account in future observational and computational studies of the spectropolarimetric structure in the Raman lines.

The importance of the direction dependent O VI emission can be determined with a detailed comparison of line structures from the O VI resonance lines with optically thin emissions from the same nebular region, like O V recombination lines (see Sect. 4.2) or the strong collisionally excited lines from Ne V, Ne VI and Mg VI. Particularly useful would be time series of these line structures covering different orbital phases.

An interesting case is AG Peg, which exhibits O VI emission from two distinct regions, from the emission nebula and from the stellar wind outflow from the hot component. Both these emissions are Raman scattered by the same scattering region. Further we know that the O VI wind region is relatively small (point-like) and centered at the position of the hot component. In principle, the comparison of the corresponding Raman scattered emissions would provide very detailed information on the structure of the O VI region. Unfortunately, the Raman scattered emission is very weak in AG Peg compared to the continuum of the red giant and only the nebular component is visible. Nonetheless, it is possible to derive a Raman scattering efficiency for the nebular region, which is at least a factor of 2 higher than that for the broad wind component. This indicates that the nebular O VI region is much closer to the cool component than the hot component. We may hope that future observations of the Raman line reveals the polarization direction of the wind component. This would define the orientation of the nebular region relative to the hot component or relative to the line connecting the two stars.

Acknowledgements. We are indebted to the support astronomers at the WHT who carried out the service observations. We thank Dr. E. Roueff for providing the data for the H_2 molecule in electronic form. This paper has benefited from many useful suggestions from an anonymous referee. The ORFEUS-SPAS missions could not have succeeded without the motivation and dedicated work of hardware groups at Berkeley, Heidelberg and Tübingen and the efficient support by NASA, DARA, DASA and Kayser Threde. This research was supported by the BMBF (DARA) grants 01 OS 8501 and 50 QV 86916. HMS acknowledges financial support by the Deutsche Forschungsgemeinschaft (KR 1053/6-1).

References

Abgrall H., Roueff E., Launay F., Roncin J.Y., Subtil J.L., 1993a, A&AS 101, 273
Abgrall H., Roueff E., Launay F., Roncin J.Y., Subtil J.L., 1993b, A&AS 101, 323
Allen D.A., 1980, MNRAS 190, 75
Altamore A., Cassatella A., 1997, A&A 317, 712
Altamore A., Baratta G.B., Cassatella A., et al., 1981, ApJ 245, 630
Aufdenberg J.P., 1993, ApJS 87, 337
Barnstedt J., Kappelmann N., Appenzeller I., et al., 1999, A&AS, 134, 561
Bastian U., 1998, A&A, 329, L61
Birriel J.J., Espey B.R., Schulte-Ladbeck R.E., 1998, ApJ 507, L75
Dumm T., Mürset U., Nussbaumer H., et al., 1998, A&A 336, 637
Espey B.R., Schulte-Ladbeck R.E., Kriss G.A., et al., 1995, ApJ 454, L61
Fernandez-Castro T., Gonzalez-Riestra R., Cassatella A., Taylor A.R., Seaquist E.R., 1995, ApJ 442, 366
Fernie J.D., 1985, PASP 97, 653
Formiggini L., Leibowitz E.M., 1994, A&A 292, 534
Friedjung M., Stencel R.E., Viotti R., 1983, A&A 126, 407

Girard T., Willson L.A., 1987, A&A 183, 247
Greiner J., Bickert K., Luthardt R., et al., 1997, A&A 322, 576
Grewing M., Appenzeller I., Barnstedt J., et al., 1998, In: Ultraviolet Astrophysics beyond the IUE Final Archive. ESA, SP-413, p. 757
Harries T.J., Howarth I.D., 1996a, A&A 310, 235
Harries T.J., Howarth I.D., 1996b, A&AS 119, 61
Harries T.J., Howarth I.D., 1997, A&AS 121, 15
Hayes M.A., Nussbaumer H., 1986, A&A 161, 287
Hummer D.G., Storey P.J., 1987, MNRAS 224, 801
Hurwitz M., Bowyer S., 1995, ApJ 446, 812
Hurwitz M., Bowyer S., Bristol R., et al., 1998, ApJ 500, L1
Iijima T., Vittone A., Chochol D., 1987, A&A 178, 203
Ivison R.J., Bode M.F., Meaburn J., 1994, A&AS 103, 201
Kafatos M., Meier S.R., Martin I., 1993, ApJS 84, 201
Kenyon S.J., Webbink R.F., 1984, ApJ 279, 252
Kenyon S.J., Mikolajewska J., Mikolajewski M., Polidan R.S., Slovak M.H., 1993, AJ 106, 1573
Keyes C.D., Plavec M., 1980, IAU Symp. 88, 535
Krautter J., Appenzeller I., Mandel H., et al., 1998, In: Ultraviolet Astrophysics beyond the IUE Final Archive. ESA, SP-413, p. 347
Lee K.W., Lee H.-W., 1997, MNRAS 292, 573
Leibowitz E.M., Formiggini L., 1992, A&A 265, 605
Li P.S., Leahy D.A., 1997, ApJ 484, 424
Massa D., 1987, AJ 94, 1675
Meinunger L., 1979, IBVS, No. 1611
Michalitsianos A.G., Kafatos M., Fahey R.P., et al., 1988, ApJ 331, 477
Mikolajewska J. (ed.), 1997, In: Mikolajewska J. (ed.) Physical Processes in Symbiotic Binaries and Related Systems. Publ. Copernicus Foundation for Polish Astronomy, Warsaw
Mikolajewska J., Kenyon S.J., 1996, AJ 112, 1659
Mikolajewska J., Kenyon S.J., Mikolajewski M., Garcia M.R., Polidan R.S., 1995, AJ 109, 1289
Morton D.C., 1975, ApJ 197, 85
Morton D.C., Dinerstein H.L., 1976, ApJ 204, 1
Mürset U., Nussbaumer H., 1994, A&A 282, 586
Mürset U., Nussbaumer H., Schmid H.M., Vogel M., 1991, A&A 248, 458
Mürset U., Jordan S., Walder R., 1995, A&A 297, L87
Mürset U., Schild H., Vogel M., 1996, A&A 307, 516
Nussbaumer H., Dumm T., 1997, A&A 323, 387
Nussbaumer H., Schild H., 1981, A&A 101, 118
Nussbaumer H., Vogel M., 1987, A&A 182, 51
Nussbaumer H., Vogel M., 1990, A&A 236, 117
Nussbaumer H., Walder R., 1993, A&A 278, 209
Nussbaumer H., Schmutz W., Vogel M., 1995, A&A 293, L13
Penston M.V., Allen D.A., 1985, MNRAS 212, 939
Penston M.V., Benvenuti P., Cassatella A., et al., MNRAS 202, 833
Rudy R.J., Cohen R.D., Rossano G.S., Puetter R.C., 1990, ApJ 362, 346
Schild H., Schmid H.M., 1996, A&A 310, 211
Schild H., Schmid H.M., 1997, A&A 324, 606
Schmid H.M., 1989, A&A 211, L31
Schmid H.M., 1990, Ph.D. Thesis No. 9187, ETH Zürich
Schmid H.M., 1995, MNRAS 275, 227
Schmid H.M., 1996, MNRAS 282, 511
Schmid H.M., 1998, Rev. in mod. Astronomy 11, 297
Schmid H.M., Nussbaumer H., 1993, A&A 268, 159
Schmid H.M., Schild H., 1990, MNRAS 246, 84
Schmid H.M., Schild H., 1994, A&A 281, 145
Schmid H.M., Schild H., 1997a, A&A 321, 791
Schmid H.M., Schild H., 1997b, A&A 327, 219
Schmid H.M., Dumm T., Mürset U., et al., 1998, A&A 329, 986
Schmutz W., 1996, In: Benvenuti P., et al. (eds.) Science with HST - II, STScI, p. 366
Seaquist E.R., Taylor A.R., Button S., 1984, ApJ 284, 202; erratum: ApJ 317, 555
Seaton M.J., 1979, MNRAS 187, 73P
Slovak M.H., Lambert D.L., 1982, in: The Nature of Symbiotic Stars. IAU Coll. 70, Reidel, p. 103
Smith V.V., Cunha K., Jorissen A., Boffin H.M.J., 1996, A&A 315, 179
Thackeray A.D., 1977, Mem. R. Astron. Soc. 83, 1
van Groningen E., 1993, MNRAS 264, 975
Van Winckel H., Duerbeck H.W., Schwarz H.E., 1993, A&AS 102, 401
Viotti R., Ricciardi O., Ponz D., et al., 1983, A&A 119, 285
Viotti R., Altamore A., Baratta G.B., Cassatella A., Friedjung M., 1984, ApJ 283, 226
Vogel M., Nussbaumer H., 1994, A&A 284, 145